Physica D 459 (2024) 134020

Contents lists available at ScienceDirect

Physica D

journal homepage: www.elsevier.com/locate/physd

Modeling vegetation patterning on sloped terrains: The role of toxic compounds

Giancarlo Consolo [a,*], Gabriele Grifó [b], Giovanna Valenti [b]

[a] Department of Mathematical, Computer, Physical and Earth Sciences, University of Messina (Italy), V.le F. Stagno D'Alcontres 31, I-98166 Messina, Italy
[b] Department of Engineering, University of Messina (Italy), C.da di Dio, I-98166 Messina, Italy

ARTICLE INFO

Keywords:
Vegetation patterning
Autotoxicity effects
Linear and multiple-scale weakly-nonlinear stability analyses
Reaction–advection–diffusion models

ABSTRACT

Vegetation patterning processes taking place on sloped terrains are here investigated through a class of three-compartments 1D reaction–advection–diffusion models enclosing the effects associated with the presence of toxic compounds. Focus is given to the transition from a uniformly-vegetated area to the desert state which occurs through the formation of an intermediate state characterized by non-stationary vegetation stripes. To this aim, linear stability analysis is addressed to characterize the mechanism of wave instability, responsible for the emergence of oscillatory Turing patterns. In detail, the analysis provides the critical value of the main control parameter as well as the wavelength and the migration speed at the onset of instability. Moreover, multiple-scale weakly nonlinear stability analysis is performed to describe the time evolution of the pattern amplitude close to the bifurcation threshold. Theoretical investigations are complemented by numerical simulations carried out for an extension of the Klausmeier kinetics that explicitly takes into account the interaction between autotoxicity and vegetation biomass. Numerical results provide several insights on how the interplay among mean annual rainfall, plant mortality and plant's sensitivity to toxicity gives rise to different ecological scenarios.

1. Introduction

In the last centuries, climate changes and human actions brought Earth to undergo abrupt shifts versus catastrophic scenarios, such as rising of global temperatures, desertification processes, more and more frequent periods of drought [1]. As a consequence of that, it is believed that dryland areas will greatly increase their extension in the very next future. To this aim, scientists have been focusing their attention on the underlying mechanisms and on the characterization of those phenomena that are considered as the precursors of the desertification of a given area. In this context, it has been widely observed that the transition from a uniformly-vegetated areas towards a bare ground is not necessarily abrupt but may occur via a sequence of patterned vegetated states, which thus represent a clear signature of ecosystem resilience [2]. Moreover, the geographical remoteness and the long timescale over which such phenomena occur make in-situ experiments quite prohibitive. Therefore, the possibility of acquiring a better understanding on the mechanisms leading to the formation and stability of vegetation patterns generally relies on mathematical models [3–24].

Most of these models agree on the "water redistribution hypothesis", the assumption through which the local biomass–water positive feedback acting at the micro-scale gives rise to spatial instabilities at the macro-scale. However, some experimental works suggested that a non-uniform vegetation cover may also arise in ecosystems where water is not the limiting resource. Among them, Mazzoleni et al. [25,26] emphasized the non-negligible role played by toxic compounds in vegetation patterning. In particular, it was proved that different phenomena act, simultaneously, at different scales and may give rise to plant–soil negative feedback: the presence of soilborne pathogens, the changing composition of soil microbial communities and the accumulation of autotoxic compounds from decomposing plant litter. This negative feedback induced by plants on soil, mainly dictated by the inhibitory effects of extracellular DNA [26], produces an increase of negative conditions for vegetation biomass that, in turn, reduces the plant growth performance.

To the best of our knowledge, the roles played by several biological parameters, such as variability and seasonality of the rainfall rate, human and/or natural effects contributing to the plant mortality, water-to-plant diffusion ratio, interspecific competition and soil carrying capacity,

* Corresponding author.
E-mail address: gconsolo@unime.it (G. Consolo).

https://doi.org/10.1016/j.physd.2023.134020
Received 31 July 2023; Received in revised form 4 December 2023; Accepted 8 December 2023
Available online 13 December 2023

have been widely investigated in two-compartments *biomass–water* models [11,15,23,27–31]. At the same time, the concept of autotoxicity in plant dynamics was firstly introduced by Marasco et al. [10,32] in a three-compartments *biomass–water–toxicity* reaction–diffusion model for *flat* environments. In these works, theoretical investigations were carried out at the onset of instability and were complemented by numerical results. For the same framework, additional investigations were addressed by Iuorio and Veerman [33] and by Spiliotis et al. [34]. The former made use of geometric singular perturbation theory to inspect far-from-threshold pulse dynamics, while the latter put particular emphasis on the symmetry breaking of vegetation bands. However, the formation of vegetation patterns along *sloped* terrains in three-compartments *biomass–water–toxicity* reaction–advection–diffusion systems, at and close to the instability threshold, has not been studied so far. This manuscript falls into this context and represents an attempt to partially fill this gap.

To this aim, let us consider a class of three-compartments 1D vegetation models that, in a suitable dimensionless form, reads:

$$\begin{cases} U_t = \mathcal{V}U_x + f(U,V), \\ V_t = V_{xx} + g(U,V,S), \\ S_t = h(V,S), \end{cases} \tag{1}$$

where $U(x,t)$, $V(x,t)$, and $S(x,t)$ represent the spatio-temporal evolution of water, biomass, and autotoxicity densities, respectively. Subscripts denote partial derivatives with respect to the indicated variable. This system encompasses a wide class of reaction–advection–diffusion systems, as it considers the following, quite general, assumptions on the compartments here considered:

- Vegetation patterning takes place along the hillslope of a given terrain. Therefore, the downhill water flow is modeled through the advection term $\mathcal{V}U_x$, being $\mathcal{V}$ the advection speed proportional to the slope gradient. Isotropic diffusion of water is considered negligibly small in comparison with anisotropic passive transport.
- The primary, isotropic, seed dispersal from the plant to the ground is mimicked by the diffusion term V_{xx}, where the diffusion coefficient is unitary, according to a suitable rescaling.
- No diffusion of toxicity is here considered, as it is fairly negligible in comparison with its decomposition processes and plant biomass dispersion [30].
- Toxicity does not directly affect water distribution and vice versa, so that the corresponding kinetic terms exhibit the functional dependencies $f(U,V)$ and $h(V,S)$.
- The release of toxic compounds and the water distribution strongly affect the spatio-temporal evolution of plant biomass, so that $g(U,V,S)$.

The content of the present manuscript can be outlined as follows.

Sections 2 and 3 are, respectively, devoted to linear and weakly nonlinear stability analyses on the general model presented in (1). In particular, the study of Turing and wave instabilities are addressed in Section 2. Here, after having proved that the occurrence of stationary Turing patterns is prevented for the considered class, emphasis is given on the critical values of the features that characterize the formation of traveling bands at onset: main control parameter, wavenumber and migration speed. On the other hand, the Stuart–Landau equation ruling the time evolution of pattern amplitude close to onset is deduced in Section 3 through a multiple-scale method. In Section 4, we propose an application of the above general framework to the case of a generalization of the Klausmeier kinetics for sloped terrains in arid environments that also accounts for the presence of toxic compounds. The analysis here carried out also includes results of numerical simulations that elucidate the combined role of rainfall rate, plant mortality and autotoxicity. Concluding remarks are given in the last section.

2. Local bifurcation analysis

In this section a linear stability analysis for the class of 1D reaction–advection–diffusion models (1) is performed in order to deduce the conditions under which the considered ecosystem may undergo a bifurcation from an uniformly-vegetated state toward a patterned configuration. This analysis will also allow us to deduce the most relevant features associated to the emerging patterns at onset.

For the sake of simplicity, let us recast system (1) in matrix form as follows:

$$\mathbf{W}_t = \mathit{\Pi}\mathbf{W}_x + \mathit{\Lambda}\mathbf{W}_{xx} + \mathbf{N}(\mathbf{W}), \tag{2}$$

being

$$\mathbf{W} = \begin{bmatrix} U \\ V \\ S \end{bmatrix}, \quad \mathit{\Pi} = \begin{bmatrix} \mathcal{V} & 0 & 0 \\ 0 & 0 & 0 \\ 0 & 0 & 0 \end{bmatrix}, \quad \mathit{\Lambda} = \begin{bmatrix} 0 & 0 & 0 \\ 0 & 1 & 0 \\ 0 & 0 & 0 \end{bmatrix}, \quad \mathbf{N}(\mathbf{W}) = \begin{bmatrix} f(U,V) \\ g(U,V,S) \\ h(V,S) \end{bmatrix}. \tag{3}$$

Let $\mathbf{W}^* = (U^*, V^*, S^*)$ be a positive spatially-homogeneous steady state admitted by the model (2)–(3) satisfying $\mathbf{N}(\mathbf{W}^*) = \mathbf{0}$ and assume $\mathcal{B}$ as a control parameter affecting the kinetic terms only.

Let us now perturb such equilibria via $\mathbf{W} = \mathbf{W}^* + \widetilde{\mathbf{W}}\exp(\omega t + \mathrm{i}kx)$, being ω the growth factor and k the wavenumber of the spatial perturbation. The resulting dispersion relation takes the form:

$$\omega^3 + A_2\omega^2 + A_1\omega + A_0 = 0 \tag{4}$$

where:

$$\begin{aligned} A_2 &= -\alpha_2 + k^2 - \mathrm{i}k\mathcal{V}, \\ A_1 &= \alpha_1 - \beta_1 k^2 + \mathrm{i}k\mathcal{V}\left(\gamma_1 - k^2\right), \\ A_0 &= \alpha_0 + f_U^* h_S^* k^2 - \mathrm{i}k\mathcal{V}\left(\gamma_0 - h_S^* k^2\right), \\ \alpha_2 &= f_U^* + g_V^* + h_S^*, \\ \alpha_1 &= f_U^* g_V^* - f_V^* g_U^* + f_U^* h_S^* + g_V^* h_S^* - h_V^* g_S^*, \\ \alpha_0 &= f_U^* g_S^* h_V^* - f_U^* g_V^* h_S^* + f_V^* g_U^* h_S^*, \\ \beta_1 &= f_U^* + h_S^*, \\ \gamma_1 &= g_V^* + h_S^*, \\ \gamma_0 &= g_V^* h_S^* - h_V^* g_S^* \end{aligned} \tag{5}$$

and the asterisk denotes that the quantity is evaluated at $\mathbf{W}^*$.

Let us now inspect about the occurrence of a Turing-type instability, namely a diffusion-driven destabilization of a spatially-uniform steady-state $\mathbf{W}^*$ that leads to a stationary spatially-periodic patterned state. To this aim, let us first adopt the Routh–Hurwitz criterion in order to determine the necessary and sufficient conditions for the local stability of $\mathbf{W}^*$ under homogeneous perturbations ($k = 0$). They read:

$$\mathrm{Re}\{\omega\} < 0 \text{ for } k = 0 \;\Leftrightarrow\; \begin{cases} f_U^* + g_V^* + h_S^* < 0, \\ f_U^* g_S^* h_V^* - f_U^* g_V^* h_S^* + f_V^* g_U^* h_S^* > 0, \\ \left(f_U^* + g_V^* + h_S^*\right)\left(f_U^* g_V^* - f_V^* g_U^* + f_U^* h_S^* + g_V^* h_S^* - h_V^* g_S^*,\right) + \\ \quad + f_U^* g_S^* h_V^* - f_U^* g_V^* h_S^* + f_V^* g_U^* h_S^* < 0. \end{cases} \tag{6}$$

However, when spatial disturbances are taken into account, a Turing bifurcation takes place if the characteristic equation admits a null eigenvalue $\omega = 0$ for a non-null wavenumber, which is tantamount of requiring in (4) that $A_0 = 0$ for $k \neq 0$. By imposing such a condition, one would get the constraint $f_U^* g_V^* h_S^* = 0$, which is incompatible with the general assumptions previously made on the functional dependence of kinetic terms. Therefore, in the considered framework, the possibility to observe stationary Turing patterns is prevented.

Therefore, let us now turn on the study of diffusion–advection-driven instability leading to oscillatory periodic patterns, i.e. traveling-wave solutions. To this aim, let us look for purely imaginary roots of the dispersion relation (4), namely $\mathrm{Re}\{\omega\} = 0$ for $k \neq 0$, and require that their real parts undergo a transition from negative to positive via a maximum. Moreover, in order to recast the perturbation in the form of a traveling wave with migration speed c, let us also assume that $\omega = -\mathrm{i}\mathsf{c}k$. Consequently, by substituting the previous ansatz into the characteristic Eq. (4) and taking its derivative with respect to k, the model (2)–(3) undergoes a wave bifurcation with critical wavenumber

$$k_c^2 = \frac{\mathcal{V}\left(g_V^* h_S^* - h_V^* g_S^*\right) + \left(f_U^* g_V^* - f_V^* g_U^* + f_U^* h_S^* + g_V^* h_S^* - h_V^* g_S^*\right)\mathsf{c}}{\mathsf{c}^3 + \mathcal{V}\mathsf{c}^2 + \left(f_U^* + h_S^*\right)\mathsf{c} + h_S^* \mathcal{V}} \tag{7}$$

for the model parameters such that

$$\begin{cases} \mathsf{c}\left(\mathcal{V} + \mathsf{c}\right)\left(\mathcal{V}\gamma_0 + \alpha_1 \mathsf{c}\right)^2 - \left(\alpha_2 \mathsf{c}^2 + \gamma_1 \mathcal{V}\mathsf{c} + f_U^* h_S^*\right)\left(\mathcal{V}\gamma_0 + \alpha_1 \mathsf{c}\right)\left(\mathsf{c}^3 + \mathcal{V}\mathsf{c}^2 + \beta_1 \mathsf{c} + h_S^* \mathcal{V}\right) + \\ \quad - \alpha_0 \left(\mathsf{c}^3 + \mathcal{V}\mathsf{c}^2 + \beta_1 \mathsf{c} + h_S^* \mathcal{V}\right)^2 = 0, \\ \left[\left(3\mathsf{c}^2 + 2\mathcal{V}\mathsf{c} + \beta_1\right) k_c^2 - \alpha_1\right]\left[\left(\alpha_2 \mathsf{c}^2 + \gamma_1 \mathcal{V}\mathsf{c} + f_U^* h_S^*\right) - 2\mathsf{c}\left(\mathcal{V} + \mathsf{c}\right) k_c^2\right] + \\ \quad + k_c^2 \left(\mathsf{c}^3 + \mathcal{V}\mathsf{c}^2 + \beta_1 \mathsf{c} + h_S^* \mathcal{V}\right)\left[\left(\mathcal{V} + 2\mathsf{c}\right) k_c^2 - 2\alpha_2 \mathsf{c} - \gamma_1 \mathcal{V}\right] = 0. \end{cases} \tag{8}$$

It should be remarked that system (8) defines implicitly the migration speed c at onset and the critical value of the control parameter $\mathcal{B}_c$ at which a wave instability occurs. Unfortunately, the nonlinear and nontrivial dependence of (8) on the model parameters prevents the possibility to extract any explicit expression that may characterize the locus at which oscillatory patterns arise. For this reason, quantitative information will be deduced via numerical investigations in the illustrative example proposed in Section 4.

3. Multiple-scale weakly-nonlinear analysis

The linear stability analysis performed in Section 2 does not allow to characterize the time evolution of the pattern amplitude close to onset. To this aim, let us perform a multiple-scale weakly-nonlinear stability analysis around the steady state $\mathbf{W}^*$ close to the critical value of the main control parameter $\mathcal{B}_c$. Therefore, let us expand the field $\mathbf{W}$ and the bifurcation parameter $\mathcal{B}$ in terms of a positive small parameter $0 < \varepsilon \ll 1$ and account for a time hierarchy as follows:

$$\begin{aligned} &\mathbf{W} = \mathbf{W}^* + \varepsilon \mathbf{W}_1 + \varepsilon^2 \mathbf{W}_2 + \varepsilon^3 \mathbf{W}_3 + O\left(\varepsilon^4\right), \\ &\mathcal{B} = \mathcal{B}_c + \varepsilon \mathcal{B}_1 + \varepsilon^2 \mathcal{B}_2 + \varepsilon^3 \mathcal{B}_3 + O\left(\varepsilon^4\right), \\ &\frac{\partial}{\partial t} \to \frac{\partial}{\partial t} + \varepsilon \frac{\partial}{\partial T_1} + \varepsilon^2 \frac{\partial}{\partial T_2} + \varepsilon^3 \frac{\partial}{\partial T_3} + O\left(\varepsilon^4\right). \end{aligned} \tag{9}$$

Then, substituting the above expansions (9) into the model (2)–(3) and collecting terms of the same orders of ε, the following set of PDEs systems is obtained:

$$\begin{aligned} &\frac{\partial \mathbf{W}_1}{\partial t} + \Pi \frac{\partial \mathbf{W}_1}{\partial x} + \Lambda \frac{\partial^2 \mathbf{W}_1}{\partial x^2} = \left[\left(\mathbf{W}_1 \cdot \nabla_{\mathbf{W}}\right)\mathbf{N}\right]_c^* && \text{at order 1} \\ &\frac{\partial \mathbf{W}_2}{\partial t} + \Pi \frac{\partial \mathbf{W}_2}{\partial x} + \Lambda \frac{\partial^2 \mathbf{W}_2}{\partial x^2} = \left[\left(\mathbf{W}_2 \cdot \nabla_{\mathbf{W}}\right)\mathbf{N}\right]_c^* + \frac{1}{2}\left[\left(\mathbf{W}_1 \cdot \nabla_{\mathbf{W}}\right)^{(2)}\mathbf{N}\right]_c^* + \mathcal{B}_1\left[\left(\mathbf{W}_1 \cdot \nabla_{\mathbf{W}}\right)\frac{\partial \mathbf{N}}{\partial \mathcal{B}}\right]_c^* - \frac{\partial \mathbf{W}_1}{\partial T_1} && \text{at order 2} \\ &\frac{\partial \mathbf{W}_3}{\partial t} + \Pi \frac{\partial \mathbf{W}_3}{\partial x} + \Lambda \frac{\partial^2 \mathbf{W}_3}{\partial x^2} = \left[\left(\mathbf{W}_2 \cdot \nabla_{\mathbf{W}}\right)\mathbf{N}\right]_c^* + \left[\left(\mathbf{W}_1 \cdot \nabla_{\mathbf{W}}\right)\left(\mathbf{W}_2 \cdot \nabla_{\mathbf{W}}\right)\mathbf{N}\right]_c^* + \mathcal{B}_2\left[\left(\mathbf{W}_1 \cdot \nabla_{\mathbf{W}}\right)\frac{\partial \mathbf{N}}{\partial \mathcal{B}}\right]_c^* + \\ &\qquad + \frac{1}{6}\left[\left(\mathbf{W}_1 \cdot \nabla_{\mathbf{W}}\right)^{(3)}\mathbf{N}\right]_c^* + \mathcal{B}_1^2\left[\left(\mathbf{W}_1 \cdot \nabla_{\mathbf{W}}\right)\frac{\partial^2 \mathbf{N}}{\partial \mathcal{B}^2}\right]_c^* + \mathcal{B}_1\left[\left(\mathbf{W}_2 \cdot \nabla_{\mathbf{W}}\right)\frac{\partial \mathbf{N}}{\partial \mathcal{B}}\right]_c^* + \\ &\qquad + \frac{1}{2}\mathcal{B}_1\left[\left(\mathbf{W}_1 \cdot \nabla_{\mathbf{W}}\right)^{(2)}\frac{\partial \mathbf{N}}{\partial \mathcal{B}}\right]_c^* - \frac{\partial \mathbf{W}_2}{\partial T_1} - \frac{\partial \mathbf{W}_1}{\partial T_2} && \text{at order 3} \end{aligned} \tag{10}$$

where the subscript "c" means that the quantity is evaluated at the bifurcating threshold, i.e. $\mathcal{B} = \mathcal{B}_c$, and the expression $\left(\mathbf{F} \cdot \nabla_{\mathbf{W}}\right)^{(j)}$, for a generic vector $\mathbf{F}$, denotes the result of applying j times the operator

$$\left(\mathbf{F} \cdot \nabla_{\mathbf{W}}\right) = F_1 \frac{\partial}{\partial U} + F_2 \frac{\partial}{\partial V} + F_3 \frac{\partial}{\partial S}. \tag{11}$$

Let us now introduce the traveling wave variable $\xi = x - \mathrm{c}t$, so that the systems (10) can be easily recast into a set of ODEs systems:

$$\begin{aligned}
&\Lambda \frac{\partial^2 \mathbf{W}_1}{\partial \xi^2} + (\Pi - \mathrm{c}\mathrm{I}) \frac{\partial \mathbf{W}_1}{\partial \xi} = \left[(\mathbf{W}_1 \cdot \nabla_{\mathbf{W}}) \mathbf{N} \right]_c^* && \text{at order 1} \\
&\Lambda \frac{\partial^2 \mathbf{W}_2}{\partial \xi^2} + (\Pi - \mathrm{c}\mathrm{I}) \frac{\partial \mathbf{W}_2}{\partial \xi} = \left[(\mathbf{W}_2 \cdot \nabla_{\mathbf{W}}) \mathbf{N} \right]_c^* + \tfrac{1}{2} \left[(\mathbf{W}_1 \cdot \nabla_{\mathbf{W}})^{(2)} \mathbf{N} \right]_c^* + \mathcal{B}_1 \left[(\mathbf{W}_1 \cdot \nabla_{\mathbf{W}}) \frac{\partial \mathbf{N}}{\partial \mathcal{B}} \right]_c^* - \frac{\partial \mathbf{W}_1}{\partial T_1} && \text{at order 2} \\
&\Lambda \frac{\partial^2 \mathbf{W}_3}{\partial \xi^2} + (\Pi - \mathrm{c}\mathrm{I}) \frac{\partial \mathbf{W}_3}{\partial \xi} = \left[(\mathbf{W}_2 \cdot \nabla_{\mathbf{W}}) \mathbf{N} \right]_c^* + \left[(\mathbf{W}_1 \cdot \nabla_{\mathbf{W}}) (\mathbf{W}_2 \cdot \nabla_{\mathbf{W}}) \mathbf{N} \right]_c^* + \mathcal{B}_2 \left[(\mathbf{W}_1 \cdot \nabla_{\mathbf{W}}) \frac{\partial \mathbf{N}}{\partial \mathcal{B}} \right]_c^* + \\
&\qquad + \tfrac{1}{6} \left[(\mathbf{W}_1 \cdot \nabla_{\mathbf{W}})^{(3)} \mathbf{N} \right]_c^* + \mathcal{B}_1^2 \left[(\mathbf{W}_1 \cdot \nabla_{\mathbf{W}}) \frac{\partial^2 \mathbf{N}}{\partial \mathcal{B}^2} \right]_c^* + \mathcal{B}_1 \left[(\mathbf{W}_2 \cdot \nabla_{\mathbf{W}}) \frac{\partial \mathbf{N}}{\partial \mathcal{B}} \right]_c^* + \\
&\qquad + \tfrac{1}{2} \mathcal{B}_1 \left[(\mathbf{W}_1 \cdot \nabla_{\mathbf{W}})^{(2)} \frac{\partial \mathbf{N}}{\partial \mathcal{B}} \right]_c^* - \frac{\partial \mathbf{W}_2}{\partial T_1} - \frac{\partial \mathbf{W}_1}{\partial T_2} && \text{at order 3}
\end{aligned} \tag{12}$$

where I is the 3×3 identity matrix.

Recasting the system $(12)_1$ into a first-order one and applying a similar procedure as the one developed in [19], the solution at the first perturbative order is given by

$$\mathbf{W}_1 = \frac{1}{2} \left\{ \Omega e^{i k_c \xi} \mathbf{d}^{(+)} + \overline{\Omega} e^{-i k_c \xi} \mathbf{d}^{(-)} \right\}, \tag{13}$$

being $\Omega = \Omega(T_1, T_2)$ the complex pattern amplitude, $\overline{\Omega}$ its conjugate and

$$\mathbf{d}^{(\pm)} = \left[\begin{array}{cccc} 1, & r_2 \pm \mathrm{i}\hat{r}_2, & r_3 \pm \mathrm{i}\hat{r}_3 \end{array} \right]^T,$$

where

$$r_2 = -f_U^*/f_V^*, \qquad \hat{r}_2 = -(\nu + \mathrm{c})\, k_c / f_V^*, \qquad r_3 = -\frac{h_V^* \left(r_2 h_S^* + \mathrm{c}\, k_c \hat{r}_2 \right)}{{h_S^*}^2 + \mathrm{c}^2 k_c^2}, \qquad \hat{r}_3 = \frac{h_V^* \left(\mathrm{c}\, k_c r_2 - \hat{r}_2 h_S^* \right)}{{h_S^*}^2 + \mathrm{c}^2 k_c^2}.$$

Note that, the complex pattern amplitude Ω remains undetermined at this stage.

By introducing (13) into the nonhomogeneous system $(12)_2$, the requirement that secular terms vanish leads to $B_1 = \frac{\partial \Omega}{\partial T_1} = 0$ so that $\Omega = \Omega(T_2)$ and the solution at the second perturbative order reads:

$$\mathbf{W}_2 = \Omega^2 e^{2 i k_c \xi} \mathbf{q} + \overline{\Omega}^2 e^{-2 i k_c \xi} \overline{\mathbf{q}} + \mathbf{q}_0 |\Omega|^2, \tag{14}$$

where the vectors $\mathbf{q} \in \mathbb{C}^3$ and $\mathbf{q}_0 \in \mathbb{R}^3$ fulfill the systems

$$\begin{aligned}
&\left[\left(\nabla_{\mathbf{W}} \mathbf{N} \right)_c^* - 2\mathrm{i} k_c (\Pi - \mathrm{c}\mathrm{I}) + 4 k_c^2 \Lambda \right] \mathbf{q} = -\tfrac{1}{8} \left[\left(\mathbf{d}^{(+)} \cdot \nabla \right)^{(2)} \mathbf{N} \right]_c^* \\
&\left(\nabla_{\mathbf{W}} \mathbf{N} \right)_c^* \mathbf{q}_0 = -\tfrac{1}{8} \left[\left(\mathbf{d}^{(+)} \cdot \nabla \right) \left(\mathbf{d}^{(-)} \cdot \nabla \right) \mathbf{N} \right]_c^*
\end{aligned} \tag{15}$$

being $\overline{\mathbf{q}}$ the complex conjugate of $\mathbf{q}$.

Finally, taking into account (13)–(14) into $(12)_3$, the elimination of resonant terms at the third perturbative order leads to the following cubic complex Stuart–Landau equation [35,36] describing the time evolution of the pattern amplitude:

$$\frac{\partial \Omega}{\partial T_2} = \left(\sigma_1 + \mathrm{i}\sigma_2 \right) \Omega - \left(L_1 - \mathrm{i} L_2 \right) |\Omega|^2 \Omega \tag{16}$$

where the coefficients here involved are not provided due to their cumbersome expressions. It should be stressed that the sign of the Landau coefficient L_1 predicts two qualitatively different dynamical regimes: supercritical, if $L_1 > 0$, or subcritical, if $L_1 < 0$. It can be noticed that (16) admits, apart from the trivial one, the nontrivial fixed point given by

$$\Omega_\infty = \sqrt{\frac{\sigma_1 + \mathrm{i}\sigma_2}{L_1 - \mathrm{i} L_2}} \tag{17}$$

that correspond to the asymptotic value of the complex pattern amplitude in the supercritical regime.

Finally, the traveling-wave solution of the governing system (2)–(3) provided by the weakly nonlinear analysis, truncated at the second-order, is expressed as:

$$\begin{aligned}
\mathbf{W}(\xi) = \mathbf{W}^* + \varepsilon &\left[\sqrt{\tfrac{\sigma_1 + \mathrm{i}\sigma_2}{L_1 - \mathrm{i} L_2}}\, e^{i k_c \xi} \mathbf{d}^{(+)} + \sqrt{\tfrac{\sigma_1 - \mathrm{i}\sigma_2}{L_1 + \mathrm{i} L_2}}\, e^{-i k_c \xi} \mathbf{d}^{(-)} \right] + \\
&+ \varepsilon^2 \left[\tfrac{\sigma_1 + \mathrm{i}\sigma_2}{L_1 - \mathrm{i} L_2} e^{2 i k_c \xi}\, \mathbf{q} + \tfrac{\sigma_1 - \mathrm{i}\sigma_2}{L_1 + \mathrm{i} L_2} e^{-2 i k_c \xi}\, \overline{\mathbf{q}} + \tfrac{\sigma_1^2 + \sigma_2^2}{L_1^2 + L_2^2}\, \mathbf{q}_0 \right] + O(\varepsilon^3).
\end{aligned} \tag{18}$$

4. A generalized Klausmeier model with plant toxicity

In this section, we discuss first a vegetation model that falls into the generalized framework (1) presented in Section 1. Then, we address numerical investigations to corroborate the theoretical findings obtained in Sections 2 and 3 as well as to investigate the role that autotoxicity plays in vegetation pattern dynamics.

Literature offers different ecological scenarios in which toxic compounds are considered within vegetation models [10,28,30,32–34]. Here, according to the hypotheses made in Section 1, an extension of the two-compartment Klausmeier model [37] has been considered. This generalization includes an extra ODE which accounts for the temporal evolution of autotoxicity and introduces additional reaction terms to describe the interaction between biomass and toxicity. In dimensional form, the 1D model reads:

$$\begin{cases}
\widetilde{U}_{\tilde{t}} = p - r \widetilde{V}^2 \widetilde{U} - l \widetilde{U} + \nu \widetilde{U}_{\tilde{x}}, \\
\widetilde{V}_{\tilde{t}} = g \widetilde{V}^2 \widetilde{U} - (d + s\widetilde{S}) \widetilde{V} + D_V \widetilde{V}_{\tilde{x}\tilde{x}}, \\
\widetilde{S}_{\tilde{t}} = q(d + s\widetilde{S}) \widetilde{V} - (k + wp) \widetilde{S},
\end{cases} \tag{19}$$

Table 1
Parameters involved in the dimensional model (19).

Parameter	Description	Units
g	Growth rate of biomass $\widetilde{V}$ due to water uptake	$m^4\ day^{-1}\ kg^{-2}$
d	Death rate of biomass $\widetilde{V}$	day^{-1}
k	Decay rate of toxicity $\widetilde{S}$	day^{-1}
l	Water loss due to evaporation or drainage	day^{-1}
p	Precipitation rate	$kg\ day^{-1}\ m^{-2}$
q	Proportion of toxins in dead biomass	–
r	Rate of water uptake	$m^4\ day^{-1}\ kg^{-2}$
s	Sensitivity of plants to toxicity $\widetilde{S}$	$m^2\ day^{-1}\ kg^{-1}$
w	Washing out of toxins by precipitation	$m^2\ kg^{-1}$
D_V	Diffusion coefficient of biomass $\widetilde{V}$	$m^2\ day^{-1}$
v	Water advection speed	$m\ day^{-1}$

where $\widetilde{U}(\tilde{x},\tilde{t})$, $\widetilde{V}(\tilde{x},\tilde{t})$, and $\widetilde{S}(\tilde{x},\tilde{t})$ are the surface water, biomass, and autotoxicity densities at location $\tilde{x}\in\Omega\subset\mathbb{R}$ (positive direction being uphill) and time $\tilde{t}\in\mathbb{R}^+$, respectively.

In (19), the downhill motion of surface water is ruled by an anisotropic transport whereas vegetation biomass diffuses isotropically. Then, water availability is characterized by a constant (mean annual) precipitation rate p and two loss terms associated to evaporation $-l\widetilde{U}$ and uptake by roots $-r\widetilde{V}^2\widetilde{U}$. On the other hand, the biomass density grows according to water availability $g\widetilde{V}^2\widetilde{U}$ and reduces because of an intrinsic mortality $-d\widetilde{V}$ and the presence of autotoxicity $-s\widetilde{S}\widetilde{V}$. Finally, the toxicity density, which is supposed not to undergo any dispersal, decreases linearly due to superposition of a decomposition rate and an implicit water washing-out effect $-(k+wp)\widetilde{S}$ whereas it increases as a consequence of the natural death of plants $qd\widetilde{V}$ and the interaction with biomass $qs\widetilde{S}\widetilde{V}$. A more detailed description of all the parameters involved in (19) is given in Table 1 [10].

To work with the simplest equivalent form of (19), let us apply the following rescaling

$$\tilde{x}=\sqrt{\frac{D_V}{l}}x,\qquad \tilde{t}=\frac{t}{l},\qquad \widetilde{U}=\frac{\sqrt{lr}}{g}U,\qquad \widetilde{V}=\sqrt{\frac{l}{r}}V,\qquad \widetilde{S}=\frac{ql\sqrt{l}}{(k+pw)\sqrt{r}}S, \tag{20}$$

and introduce the non-dimensional parameters

$$\begin{aligned}&\mathcal{A}=\tfrac{gp}{l\sqrt{lr}},\qquad \mathcal{B}=\tfrac{d}{l},\qquad \mathcal{D}=\tfrac{l}{k+pw},\\ &\mathcal{H}=\tfrac{sq\sqrt{l}}{(k+pw)\sqrt{r}},\qquad \mathcal{V}=\tfrac{v}{\sqrt{D_B l}}.\end{aligned} \tag{21}$$

Here, $\mathcal{A}$ is related to the mean annual rainfall, $\mathcal{B}$ to the plant mortality, $\mathcal{V}$ to the slope of the terrain, $\mathcal{H}$ to the plant's sensitivity to toxicity and $\mathcal{D}$ to the decomposition rate of toxic compounds. Taking into account (20) and (21), model (19) can be recast in non-dimensional form:

$$\begin{cases} U_t=\mathcal{A}-U-V^2U+\mathcal{V}U_x,\\ V_t=V^2U-\mathcal{B}V-\mathcal{H}SV+V_{xx},\\ \mathcal{D}S_t=\mathcal{B}V+\mathcal{H}SV-S.\end{cases} \tag{22}$$

It can be easily noticed that, for $\mathcal{H}=0$, the original Klausmeier model is recovered and the autotoxicity effect on plant biomass vanishes.

In order to gain some insights into vegetation patterning along sloped drylands, let us go first through the results of linear stability analysis drawn in Section 2. The spatially-homogeneous steady-states $\mathbf{W}^*\equiv(U^*,V^*,S^*)$ admitted by (22) depend upon the rainfall $\mathcal{A}$, the plant loss $\mathcal{B}$ and the plant's sensitivity to toxicity $\mathcal{H}$, namely

$$\begin{aligned}&\mathcal{A}<\mathcal{A}_{ex}\quad\Rightarrow\quad\text{desert state}\qquad \mathbf{W}^*_D\equiv(\mathcal{A},0,0)\\ &\mathcal{A}>\mathcal{A}_{ex}\quad\Rightarrow\quad\text{three equilibria}\qquad \mathbf{W}^*_D,\ \mathbf{W}^*_{R,L}=\left(\tfrac{\mathcal{B}}{V_{R,L}(1-\mathcal{H}V_{R,L})},\quad V_{R,L},\quad \tfrac{\mathcal{B}V_{R,L}}{1-\mathcal{H}V_{R,L}}\right),\end{aligned} \tag{23}$$

with

$$\begin{aligned}&\mathcal{A}_{ex}=2\mathcal{B}\left(\mathcal{H}+\sqrt{1+\mathcal{H}^2}\right),\\ &0<V_L=\tfrac{\mathcal{A}-\sqrt{\mathcal{A}^2-4\mathcal{B}(\mathcal{B}+\mathcal{A}\mathcal{H})}}{2(\mathcal{B}+\mathcal{A}\mathcal{H})}<\sqrt{1+\mathcal{H}^2}-\mathcal{H}<V_R=\tfrac{\mathcal{A}+\sqrt{\mathcal{A}^2-4\mathcal{B}(\mathcal{B}+\mathcal{A}\mathcal{H})}}{2(\mathcal{B}+\mathcal{A}\mathcal{H})}.\end{aligned} \tag{24}$$

In particular, when $\mathcal{A}=\mathcal{A}_{ex}$ the steady-states $\mathbf{W}^*_R$ and $\mathbf{W}^*_L$ coincide with each other being $V_R=V_L=\sqrt{1+\mathcal{H}^2}-\mathcal{H}$.

Then, the terms appearing in the dispersion relation (4) become

$$\begin{aligned}\alpha_2&=-\left(1+V^{*2}\right)+2U^*V^*-\mathcal{B}-\mathcal{H}S^*+\tfrac{1}{\mathcal{D}}\left(\mathcal{H}V^*-1\right),\\ \alpha_1&=\left(\tfrac{\mathcal{H}V^*-1}{\mathcal{D}}-1-V^{*2}\right)\left(2U^*V^*-\mathcal{B}-\mathcal{H}S^*\right)+2U^*V^{*3}+\tfrac{1}{\mathcal{D}}\left(1+V^{*2}\right)+\tfrac{\mathcal{H}V^*}{\mathcal{D}}\left(\mathcal{B}+\mathcal{H}S^*-1-V^{*2}\right),\\ \alpha_0&=\tfrac{1}{\mathcal{D}}\left\{\left(1+V^{*2}\right)\left[\mathcal{H}V^*\left(\mathcal{B}+\mathcal{H}S^*\right)+\left(2U^*V^*-\mathcal{B}-\mathcal{H}S^*\right)\left(\mathcal{H}V^*-1\right)\right]-2U^*V^{*3}\left(\mathcal{H}V^*-1\right)\right\},\\ \beta_1&=\tfrac{1}{\mathcal{D}}\left(\mathcal{H}V^*-1\right)-1-V^{*2},\\ \beta_0&=\tfrac{1}{\mathcal{D}}\left(1+V^{*2}\right)\left(1-\mathcal{H}V^*\right)\\ \gamma_1&=2U^*V^*-\mathcal{B}-\mathcal{H}S^*+\tfrac{1}{\mathcal{D}}\left(\mathcal{H}V^*-1\right),\\ \gamma_0&=\tfrac{1}{\mathcal{D}}\left(\mathcal{H}V^*-1\right)\left(2U^*V^*-\mathcal{B}-\mathcal{H}S^*\right)+\tfrac{\mathcal{H}V^*}{\mathcal{D}}\left(\mathcal{B}+\mathcal{H}S^*\right).\end{aligned} \tag{25}$$

where the components of the jacobian matrix $\nabla_{\mathbf{W}}\mathbf{N}$, evaluated at each steady state (23), take the form:

$$\begin{gathered}
f_U(\mathbf{W}_D^*)=-1,\quad f_V(\mathbf{W}_D^*)=0,\quad h_V(\mathbf{W}_D^*)=\frac{\mathcal{B}}{\mathcal{D}},\quad h_S(\mathbf{W}_D^*)=-\frac{1}{\mathcal{D}},\\
g_U(\mathbf{W}_D^*)=0,\quad g_V(\mathbf{W}_D^*)=-\mathcal{B},\quad g_S(\mathbf{W}_D^*)=0,\\
f_U(\mathbf{W}_{R,L}^*)=-\left(1+V_{R,L}^2\right),\quad f_V(\mathbf{W}_{R,L}^*)=-\frac{2\mathcal{B}}{1-\mathcal{H}V_{R,L}},\quad h_V(\mathbf{W}_{R,L}^*)=\frac{\mathcal{B}}{\mathcal{D}(1-\mathcal{H}V_{R,L})},\quad h_S(\mathbf{W}_{R,L}^*)=\frac{\mathcal{H}V_{R,L}-1}{\mathcal{D}},\\
g_U(\mathbf{W}_{R,L}^*)=V_{R,L}^2,\quad g_V(\mathbf{W}_{R,L}^*)=\frac{\mathcal{B}}{1-\mathcal{H}V_{R,L}},\quad g_S(\mathbf{W}_{R,L}^*)=-\mathcal{H}V_{R,L},
\end{gathered}\tag{26}$$

To investigate the local stability of the steady-states against homogeneous perturbations, let us apply conditions (6) to the considered case. It can be proven that the desert state $\mathbf{W}_D^*$ is always stable, the vegetated state $\mathbf{W}_L^*$ is always unstable whereas the stability of the steady state $\mathbf{W}_R^*$ depends on the model parameters and results to be locally stable iff the following conditions are met:

$$\begin{cases}
V_R^2+1-\frac{\mathcal{B}}{1-\mathcal{V}V_R}+\frac{1-\mathcal{H}V_R}{\mathcal{D}}>0\\
\left[\mathcal{B}-\left(1+V_R^2\right)\left(1-\mathcal{H}V_R\right)\right]\left[\left(\mathcal{H}V_R-1\right)^2\left(\mathcal{H}V_R-1\right)-2\mathcal{B}\mathcal{D}^2V_R^2\right]+\\
\quad+\left[\mathcal{B}\mathcal{D}-\left(1-\mathcal{H}V_R\right)^2\right]\left[-\mathcal{B}\mathcal{H}V_R-\mathcal{D}\left(1-\mathcal{H}V_R\right)\left(1+V_R\right)^2\right]+\\
\quad-\mathcal{B}\mathcal{D}\left\{\mathcal{B}\left[\mathcal{H}V_R-1-\mathcal{D}\left(1+V_R^2\right)\right]+2\left(1-\mathcal{H}V_R\right)^2\left(V_R+1\right)\right\}>0.
\end{cases}\tag{27}$$

By reminding that Turing patterns are not allowed in the present model, let us focus on the occurrence of wave bifurcations that give rise to oscillatory pattern dynamics starting from a stable homogeneous steady-state. For this reason, the only candidate for this analysis is the vegetated state $\mathbf{W}_R^*$. In fact, the need of guaranteeing the positiveness of the solution prevents oscillations about the desert state $\mathbf{W}_D^*$, whereas the vegetated state $\mathbf{W}_L^*$ is always locally unstable.

With this in mind, by considering the plant loss $\mathcal{B}$ as the main control parameter, oscillatory periodic patterns arise with a critical wavenumber (7) that specializes into:

$$k_c^2=\frac{\mathcal{V}\mathcal{B}\left(2\mathcal{H}V_{R_c}-1\right)+\left[\mathcal{B}\mathcal{D}\left(V_{R_c}^2-1\right)-\mathcal{B}\left(1-\mathcal{H}V_{R_c}\right)+\left(1+V_{R_c}^2\right)\left(1-\mathcal{H}V_{R_c}\right)^2\right]\mathsf{c}}{\left(1-\mathcal{H}V_{R_c}\right)\left\{\mathcal{D}\mathsf{c}^3+\mathcal{V}\mathcal{D}\mathsf{c}^2+\left[\mathcal{H}V_{R_c}-1-\mathcal{D}\left(1-V_{R_c}\right)\right]\mathsf{c}+\mathcal{V}\left(\mathcal{H}V_{R_c}-1\right)\right\}}\tag{28}$$

where $V_{R_c}=\left[\mathcal{A}+\sqrt{\mathcal{A}^2-4\mathcal{B}_c\left(\mathcal{B}_c+\mathcal{A}\mathcal{H}\right)}\right]/\left[2\left(\mathcal{B}_c+\mathcal{A}\mathcal{H}\right)\right]$. On the other hand, the critical values of the bifurcating parameter $\mathcal{B}_c$ and the migration speed at the onset of instability are implicitly defined by (8), (25), (26). These quantities will be now computed numerically in order to better elucidate the role of plant autotoxicity in oscillatory vegetated band dynamics. To address this issue in more detail, let us focus on how the parameter $\mathcal{H}$, which measures the plant's sensitivity to toxicity, affects the main features of the emerging patterns.

In Fig. 1, the bifurcation diagram in the $(\mathcal{B},\mathcal{A})$ parameter plane (panel (a)) and the critical wavenumber dependence on the critical plant loss $\mathcal{B}_c$ (panel (b)) are plotted for different values of $\mathcal{H}$, by keeping the slope gradient and the toxicity-induced decomposition rate fixed at $\mathcal{V}=182.5$ and $\mathcal{D}=4.5$, respectively. Note that, in panel (a), the solid lines represent the wave instability loci whereas the dashed ones depict the existence loci $\mathcal{A}=\mathcal{A}_{ex}(24)_1$ below which the only desert state exists and is stable. The region between these loci represent the prediction region where oscillatory patterns, in the form of migrating vegetation stripes, can be observed. Our theoretical results predict that the increase of plant's sensitivity to toxicity carries a twofold effect: it shifts up both wave bifurcation and existence loci. However, the effect is much more remarkable for the wave locus, with the consequence that toxicity yields an overall enlargement of the portion of the parameter plane where pattern may arise (and, in turn, a relatively small increase of the desert state region), namely a destabilizing effect on the uniformly-vegetated steady state. From the ecological viewpoint, autotoxicity has an inhibitory effect on the growth of plants due to the release of toxic chemicals into the environment. This phenomenon causes the soil sickness and, in turn, a reduction of the overall vegetation cover. As a consequence of that, the introduction of such a stressor acts on the environment by favoring transitions from a uniformly vegetated state to a patterned one or from a patterned configuration to desert. On the other hand, panel (b) gives information about the stripe wavelength. In particular, it is found that larger wavenumbers, i.e. smaller wavelengths, are excited at onset with the increase of $\mathcal{H}$.

In order to validate the analytical predictions reported in Fig. 1(a), let us integrate numerically the governing system (22) by means of a finite-element framework COMSOL Multiphysics® [38] over a spatial domain $x\in[0,x_D]$ (with $x_D=100$) together with periodic boundary conditions and setting a small random perturbation of the spatially-homogeneous steady state $\mathbf{W}_R^*$ as initial configuration. To this aim, let us then consider four different points in the $(\mathcal{B},\mathcal{A})$ parameter plane, denoted by P_i with $i=1,\dots,4$, characterized by a fixed rainfall rate ($\mathcal{A}=2.5$) and different plant loss $\mathcal{B}$ values. In particular, let us assume that $\mathcal{B}$ increases over time according to a piecewise function as denoted in Fig. 2(a), so mimicking a possible variability of plant mortality due to climate changes, pollution effects or grazing events. Note that, since the linear stability analysis here performed is valid for time-independent parameters only, numerical results should be compared with analytical ones only if, at each step, the model (22) is taken into account with a fixed plant loss $\mathcal{B}$. To inspect the role of plant toxicity, let us also consider three values for the coefficient $\mathcal{H}=0$, 0.02 and 0.05. Other model parameters are set as in Fig. 1.

Numerical results shown in Fig. 2(b–d) reveal that the points P_i may lie in the wave instability region or not, depending on the value of plant's sensitivity to toxicity $\mathcal{H}$, in agreement with theoretical predictions reported in Fig. 1(a). Indeed, when autotoxicity is neglected ($\mathcal{H}=0$, see Fig. 2(b)), the system is able to give rise to oscillatory periodic patterns at the configuration P_4 only, which corresponds to the largest considered value of plant mortality ($\mathcal{B}=0.4$). When $\mathcal{H}=0.02$ (Fig. 2(c)), migrating bands are observed starting from P_3 ($\mathcal{B}=0.35$), whereas for $\mathcal{H}=0.05$ (Fig. 2(d)), patterns originate from P_2 ($\mathcal{B}=0.3$), namely for progressively smaller plant loss values as toxicity is increased. These observations confirm, again, that the noxious effect of plant autotoxicity destabilizes the spatially-homogeneous steady state by favoring the formation of a patterned state that, in turn, marks a route towards desertification.

To better elucidate the role of toxicity, let us inspect in more detail the profile of vegetation biomass $V(x,t_{end})$, toxicity $S(x,t_{end})$ and surface water $U(x,t_{end})$ obtained for $\mathcal{H}=0.05$ and for fixed values of rainfall $\mathcal{A}$ and plant loss $\mathcal{B}$ corresponding to the point P_4 depicted in Fig. 1(a) (here,

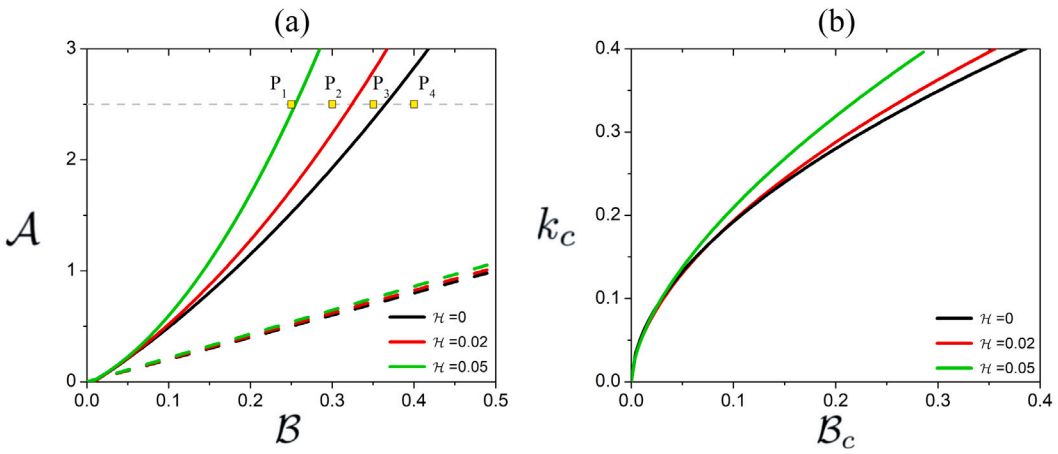

Fig. 1. (a) Bifurcation diagram in the $(\mathcal{B}, \mathcal{A})$-plane and (b) critical wavenumber k_c as a function of B_c for different values of plant's sensitivity toxicity $\mathcal{H}$. In (a), the wave bifurcation loci are denoted by solid lines, whereas the dashed ones represent the loci $\mathcal{A} = \mathcal{A}_{ex}$ defined in $(24)_1$. Yellow squares depict the configurations $P_1 = (0.25, 2.5)$, $P_2 = (0.30, 2.5)$, $P_3 = (0.35, 2.5)$ and $P_4 = (0.40, 2.5)$, respectively. Fixed parameters: $\mathcal{V} = 182.5$ and $D = 4.5$.

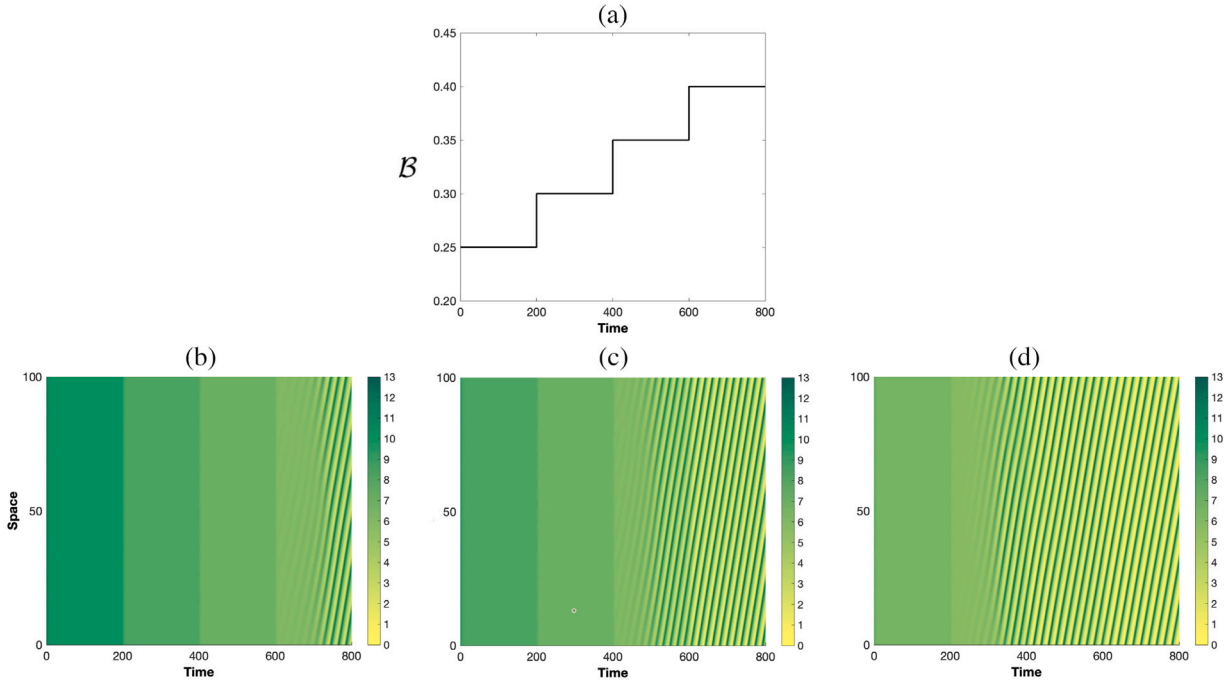

Fig. 2. Spatio-temporal dynamics of vegetation biomass $V(x,t)$ corresponding to the ecological scenario reported in panel (a) for $\mathcal{H} = 0$ (b), $\mathcal{H} = 0.02$ (c) and $\mathcal{H} = 0.05$ (d). Other parameters as in Fig. 1.

$t_{end} = 800$ represents the ending simulation time). Results depicted in Fig. 3 reveal that the peak of toxicity is shifted with respect to the one of biomass and, more noteworthy, the biomass production at the edges of each vegetated stripe is reduced in a non-symmetric way. In particular, the lower edge of the patch is eroded more deeply because of the larger amount of toxic compounds there localized, whereas the upper edge undergoes a smoother erosion because it feels the tail of toxicity associated to the adjacent pattern moving uphill. The outcome of this toxicity-driven process is an overall narrowing of vegetation bands. This is fully justifiable from the ecological viewpoint as the introduction of toxicity-induced plant loss acts as a plant–soil negative feedback that disfavors uniform distributions of biomass. Indeed, since this additional ecosystem stressor yields the accumulation of dead biomass and its consequent decomposition, the consequent release of autotoxic compounds reduces the plant growth performance [28].

To gain additional information on the migrating vegetation bands at the onset of instability, let us investigate how the wave speed c is affected by autotoxicity. To this aim, system (7), (8) is solved numerically by allowing $\mathcal{H} \in [0, 0.05]$ and varying rainfall $\mathcal{A}$ and plant loss $\mathcal{B}$ along the corresponding wave bifurcation locus. Results reported in Fig. 4 point out that plant's sensitivity to toxicity, apart from affecting the wave bifurcation locus, may strongly affect the migration speed. For instance, if the rainfall rate is kept fixed at $\mathcal{A} = 3$, the autotoxicity yields an increase of the pattern mobility from 0.8 to 1.2, i.e. up to 50%. On the other hand, from the ecological viewpoint an increase in rainfall rate represents a larger

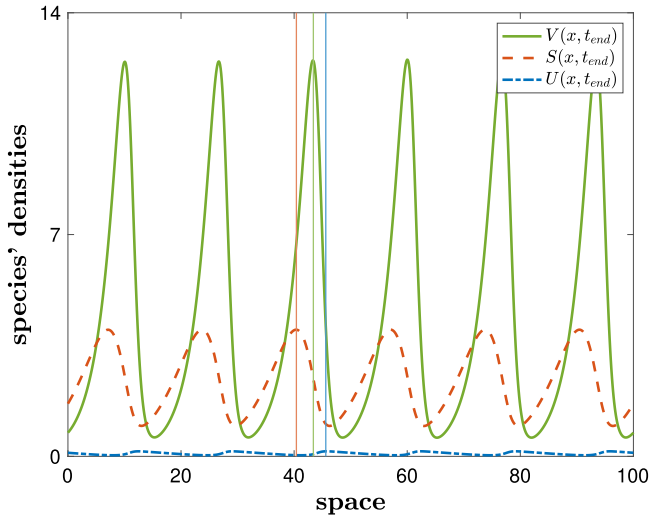

Fig. 3. Spatial profiles of vegetation biomass $V(x,t)$, autotoxicity $S(x,t)$ and surface water $U(x,t)$ evaluated at $t = t_{end} = 800$. Vertical lines are drawn as guide-to-eye, to emphasize the spatial shift between the peaks. Parameter values: $\mathcal{A} = 2.5$, $\mathcal{H} = 0.05$, $\mathcal{V} = 182.5$, $\mathcal{D} = 4.5$ and $\mathcal{B} = 0.40$.

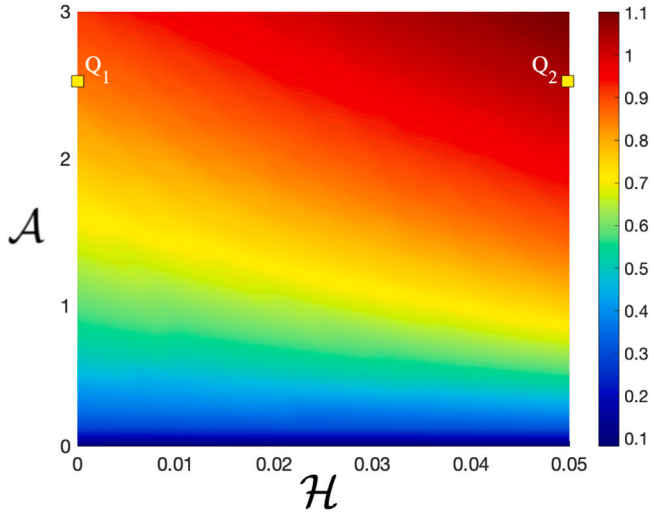

Fig. 4. Density-plot showing the level curves in the $(\mathcal{H}, \mathcal{A})$-plane for the migration speed c at the onset of instability $\mathcal{B} = \mathcal{B}_c$. Yellow squares depict the configurations $Q_1 = (0, 2.5)$ and $Q_2 = (0.05, 2.5)$, respectively. Other parameters as in Fig. 1.

availability of water that converts into higher levels of accumulation of soil moisture in the top part of vegetation bands. This phenomenon leads to more favorable conditions for the uphill motion of vegetation biomass and, thus, to higher migration speeds [5,13].

In order to corroborate these results, let us integrate numerically the governing system (22) over the time window $t \in [0, 500]$ and the spatial domain $x \in [0, x_D]$ by setting the parameters $\mathcal{A}$ and $\mathcal{H}$ as denoted by the points Q_1 and Q_2 in Fig. 4 whereas the plant loss is chosen in such a way that, in both cases, the distance from the threshold is kept fixed at $\varepsilon^2 = 10^{-2}$. The snapshots of the resulting simulations are reported in Fig. 5(a, d)). Then, to extract the critical features that characterize the migration process, namely the angular frequency ω and the wavenumber k, let us apply two Fast Fourier Transforms (FFTs) on the biomass $V(x,t)$ by fixing either space or time. In particular, we first consider $V(x,t)$ at $x = x_D/2$ and perform FFT over time (see Fig. 5(b, e)) and, then, evaluate biomass at $t = t_{end}$ applying FFT over space (see Fig. 5(c, f)). As it can be observed, the spectra so obtained consist of a main peak and several higher-order harmonics due to the slow modulation of the pattern close to the onset [39]. By identifying the main peaks as the critical angular frequency ω_c and wavenumber k_c, respectively, accounting for the ansatz made in Section 2, the wave speed at the onset of instability can be easily obtained via $c = \omega_c/k_c$. The comparison between numerical results arising from Fig. 5 and analytical ones depicted in Fig. 4 reveals a satisfying agreement. Indeed, as far as configuration Q_1 is concerned, $c_{num} = 0.32/0.37 = 0.86$ and $c_{ana} = 0.85$; whereas at Q_2, $c_{num} = 0.35/0.32 = 1.09$ and $c_{ana} = 1.06$. Results here obtained validate further the theoretically-achieved conclusion on the non-negligible role played by the plant's sensitivity to autotoxicity $\mathcal{H}$.

The investigations carried out so far have focused on the theoretical predictions arising from linear stability analysis addressed in Section 2. Let us now extract additional information from the multiple-scale weakly nonlinear analysis developed in Section 3 and, in particular, on the pattern amplitude close to the onset of instability. For the considered generalized Klausmeier model which includes auto-toxicity effects, the coefficients

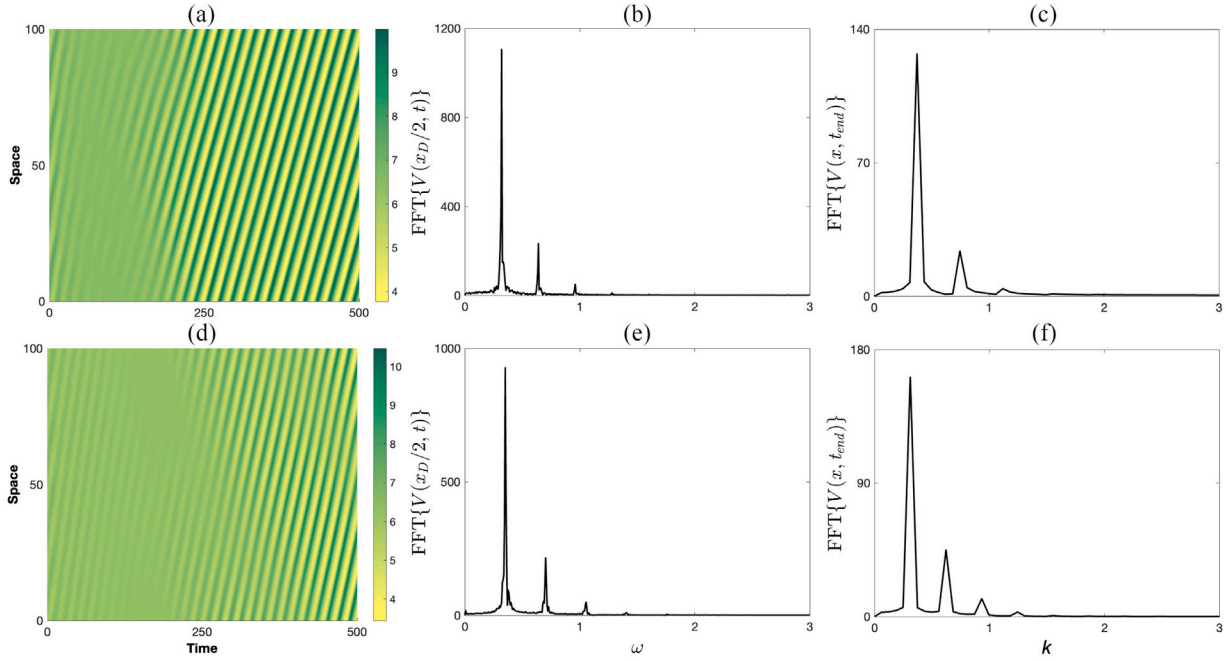

Fig. 5. (a, d) Snapshots of oscillatory vegetation patterns. (b, e) FFT of the time-dependent solution $V(x,t)$ evaluated at $x = x_D/2$. (c, f) FFT of the space-dependent solution $V(x,t)$ evaluated at $t = t_{end}$. Panels in the top (bottom) row are obtained by using the parameter set corresponding to point Q_1 (Q_2) depicted in Fig. 4 and considering a distance from the threshold equal to $\epsilon^2 = 10^{-2}$.

appearing in the cubic complex Stuart–Landau equation (16) take the explicit form:

$$
\begin{aligned}
\sigma_1 = \mathcal{B}_2 \Bigg\{ & \frac{c\left(\left.\frac{df_U^*}{d\mathcal{B}}\right|_c + \left.\frac{df_V^*}{d\mathcal{B}}\right|_c r_2\right)(n_5n_8 - n_6n_7) + \left(\left.\frac{dg_S^*}{d\mathcal{B}}\right|_c r_4 + \left.\frac{dg_U^*}{d\mathcal{B}}\right|_c + \left.\frac{dg_V^*}{d\mathcal{B}}\right|_c r_2\right)(n_3n_8 + n_1n_7) - \left(\left.\frac{dh_S^*}{d\mathcal{B}}\right|_c r_4 + \left.\frac{dh_V^*}{d\mathcal{B}}\right|_c r_2\right)(n_4n_8 + n_2n_7)}{n_7^2 + n_8^2} + \\
& + \frac{\left(\left.\frac{dh_S^*}{d\mathcal{B}}\right|_c \hat{r}_4 + \left.\frac{dh_V^*}{d\mathcal{B}}\right|_c \hat{r}_2\right)(n_4n_7 - n_2n_8) - c\left.\frac{df_V^*}{d\mathcal{B}}\right|_c \hat{r}_2(n_5n_7 + n_6n_8) + \left(\left.\frac{dg_S^*}{d\mathcal{B}}\right|_c \hat{r}_4 + \left.\frac{dg_V^*}{d\mathcal{B}}\right|_c \hat{r}_2\right)(n_1n_8 - n_3n_7)}{n_7^2 + n_8^2} \Bigg\}, \\
\sigma_2 = \mathcal{B}_2 \Bigg\{ & \frac{c\left(\left.\frac{df_U^*}{d\mathcal{B}}\right|_c + \left.\frac{df_V^*}{d\mathcal{B}}\right|_c r_2\right)(n_5n_7 - n_6n_8) + \left(\left.\frac{dg_S^*}{d\mathcal{B}}\right|_c r_4 + \left.\frac{dg_U^*}{d\mathcal{B}}\right|_c + \left.\frac{dg_V^*}{d\mathcal{B}}\right|_c r_2\right)(n_3n_7 + n_1n_8) - \left(\left.\frac{dh_S^*}{d\mathcal{B}}\right|_c r_4 + \left.\frac{dh_V^*}{d\mathcal{B}}\right|_c r_2\right)(n_4n_7 + n_2n_8)}{n_7^2 + n_8^2} + \\
& + \frac{\left(\left.\frac{dh_S^*}{d\mathcal{B}}\right|_c \hat{r}_4 + \left.\frac{dh_V^*}{d\mathcal{B}}\right|_c \hat{r}_2\right)(n_4n_8 - n_2n_7) - c\left.\frac{df_V^*}{d\mathcal{B}}\right|_c \hat{r}_2(n_5n_8 + n_6n_7) + \left(\left.\frac{dg_S^*}{d\mathcal{B}}\right|_c \hat{r}_4 + \left.\frac{dg_V^*}{d\mathcal{B}}\right|_c \hat{r}_2\right)(n_1n_7 - n_3n_8)}{n_7^2 + n_8^2} \Bigg\}, \\
L_1 = & \frac{c\,m_1(n_5n_8 - n_6n_7) + m_2(n_3n_8 + n_1n_7) + m_3(n_4n_8 + n_2n_7) + m_4(n_4n_7 - n_2n_8) + c\,m_5(n_5n_7 + n_6n_8) + m_6(n_1n_8 - n_3n_7)}{n_7^2 + n_8^2}, \\
L_2 = & \frac{c\,m_1(n_5n_7 - n_6n_8) + m_2(n_3n_7 + n_1n_8) + m_3(n_4n_7 + n_2n_8) + m_4(n_4n_8 - n_2n_7) + c\,m_5(n_5n_8 + n_6n_7) + m_6(n_1n_7 - n_3n_8)}{n_7^2 + n_8^2},
\end{aligned}
\tag{29}
$$

where the expressions of the quantities here involved are reported in Appendix.

As already mentioned, the sign of the real part of the Landau coefficient characterizes the dynamical regime: supercritical if $L_1 > 0$ and subcritical if $L_1 < 0$. Let us firstly inspect how the parameter L_1 is affected by rainfall A and autotoxicity $\mathcal{H}$, at the onset of instability $\mathcal{B} = \mathcal{B}_c$. Results are depicted in Fig. 6, where the region colored in green represents the supercritical behavior whereas the white one denotes the subcritical regime. Theoretical predictions reveal that, when the interaction between plant and toxicity is ignored $\mathcal{H} = 0$, there exists a range of rainfall values in which dynamics occurs in the subcritical regime. This interval progressively shrinks as the plant's sensitivity to toxicity is increased.

To validate such results, let us consider two configurations in the $(\mathcal{H}, \mathcal{A})$-plane, denoted by $\mathrm{Q}_3 = (0, 0.75)$ and $\mathrm{Q}_4 = (0.05, 0.75)$, and integrate numerically the governing system (22) over a spatial domain $x \in [0, 500]$ for Q_3 or $x \in [0, 100]$ for Q_4. The larger domain in the former case is dictated by the fact that larger wavelengths are generally expected in the subcritical case. In this analysis, to inspect the possible occurrence of hysteresis, let us vary the plant loss $\mathcal{B}$ as depicted in Fig. 7(a). In particular, for $t \in [0, 1000]$, the system is driven, in both cases, towards a patterned configuration being $\mathcal{B} > \mathcal{B}_c$. For $t \in [1000, 2000]$, the plant loss is reduced down to a slightly-below threshold value $\mathcal{B} < \mathcal{B}_c$. In this time window, at Q_3, patterns still survive (see Fig. 7(b)), so denoting the hysteretic character which confirms the subcritical nature of the observed patterns. On the contrary, at Q_4, patterns undergo a smooth transition towards the uniformly-vegetated state, that clearly points out its supercritical nature (see Fig. 7(c)). In the third time window, $t \in [2000, 3000]$, the plant loss value is decreased further (value $\mathcal{B}_s$) in order to get the extinction of patterns at

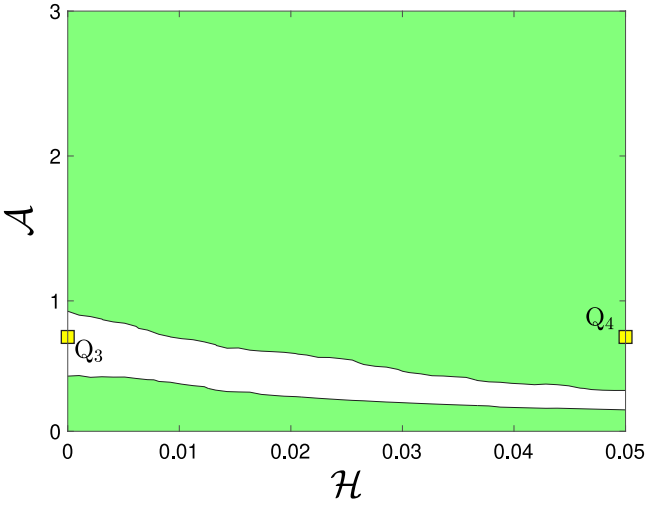

Fig. 6. Contour plot of the Landau coefficient L_1 as a function of the plant's sensitivity to toxicity $\mathcal{H}$ and the rainfall rate $\mathcal{A}$. Colored (white) areas denote positive (negative) values of L_1. Yellow squares depict the configurations in the $(\mathcal{H}, \mathcal{A})$-plane given by $Q_3 = (0, 0.75)$ and $Q_4 = (0.05, 0.75)$, respectively. Other parameters as in Fig. 1.

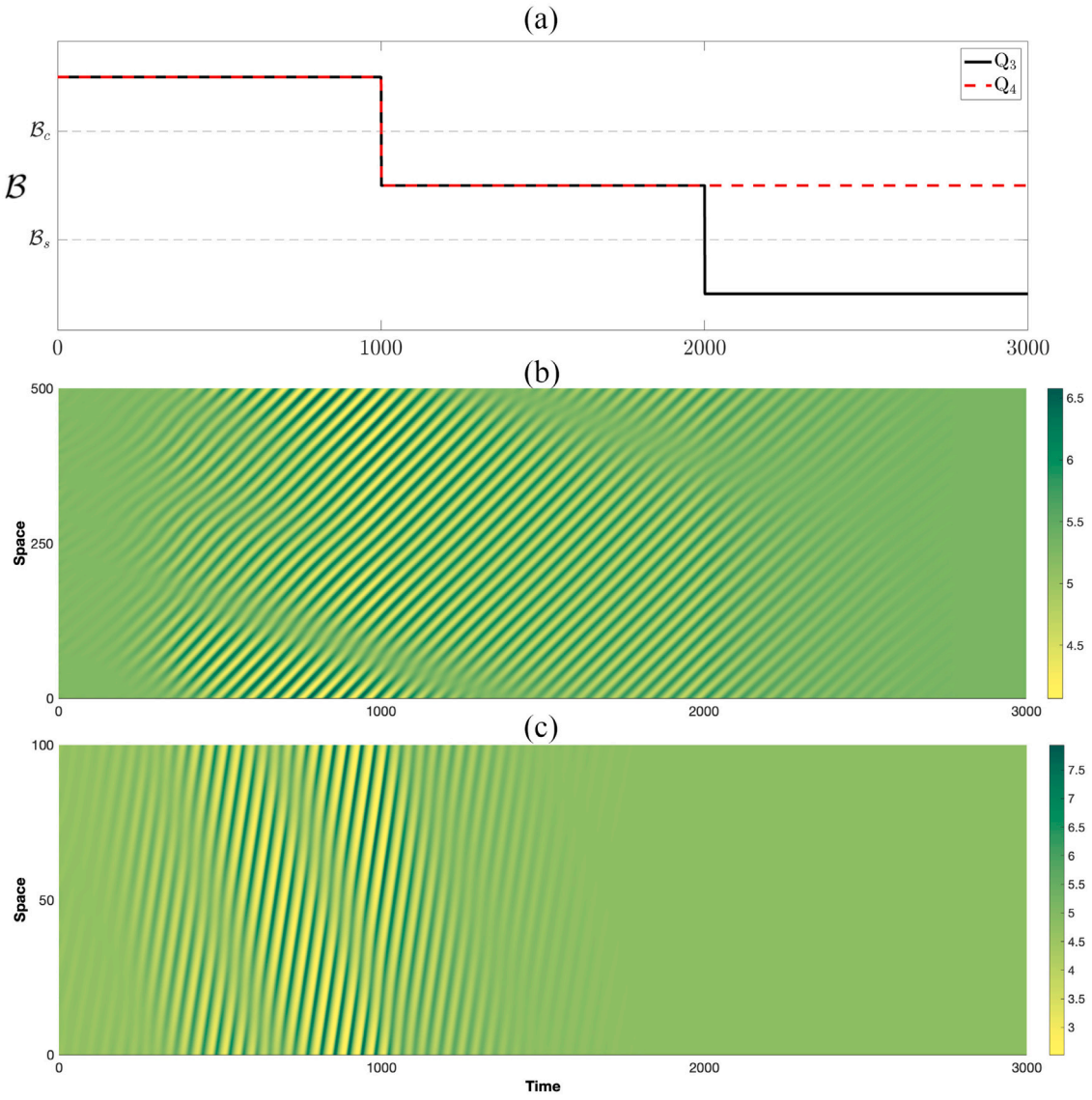

Fig. 7. Spatio-temporal dynamics of vegetation biomass $V(x, t)$ corresponding to the ecological scenario in which the plant loss $\mathcal{B}$ is varied as reported in panel (a). Results are representative of the configurations in the $(\mathcal{H}, \mathcal{A})$ plane denoted by (b) Q_3 and (c) Q_4 and reported in Fig. 6. Other parameters as in Fig. 1.

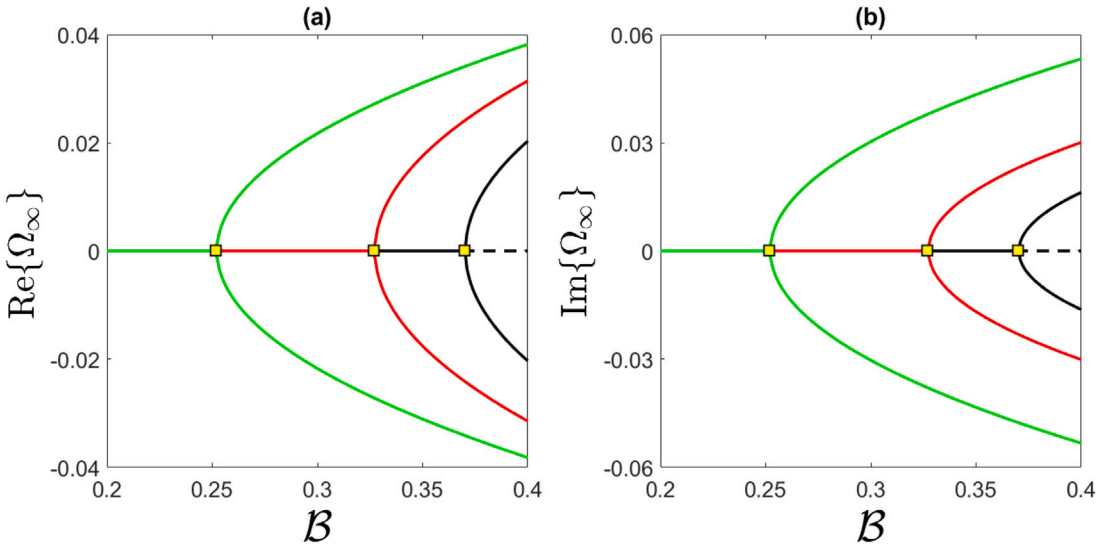

Fig. 8. Supercritical bifurcation diagrams of the (a) real and (b) imaginary part of the complex amplitude Ω obtained analytically via (16), for $\mathcal{H} = 0$ (black solid line), $\mathcal{H} = 0.02$ (red solid line), and $\mathcal{H} = 0.05$ (green solid line). Solid lines denote stable branches, dashed lines unstable ones. Fixed parameters: $\mathcal{A} = 2.5$, $\mathcal{V} = 182.5$, $\mathcal{D} = 4.5$.

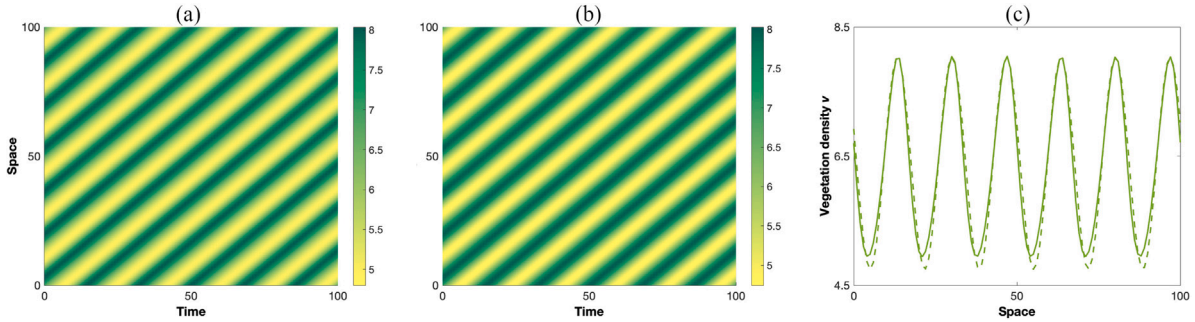

Fig. 9. (a) Numerically-computed solution obtained by integrating the governing system (22). (b) Theoretical solution deduced from weakly-nonlinear analysis (18). (c) Comparison between the solutions depicted in panels (a) and (b) for $t = t_{end}$. Fixed parameters: $\mathcal{A} = 2.5$, $\mathcal{H} = 0.05$, $\mathcal{V} = 182.5$, $\mathcal{D} = 4.5$ and $\mathcal{B} = 0.26$.

Q_3 too. From the ecological viewpoint, it is possible to draw the conclusion that, at least in the considered parameter setup, the plant's sensitivity to toxicity makes the system less resilient to variations of plant loss.

Let us now focus on the validity of the analytical solution deduced from the multiple-scale method up to the second order approximation (18). For simplicity, let us limit the analysis to the supercritical regime only ($L_1 > 0$). As observed in (17), (29), the asymptotic complex pattern amplitude Ω_∞ is strongly affected by the model parameters and, in particular, by autotoxicity effects. To investigate quantitatively this phenomenon, let us build in Fig. 8 the bifurcation diagrams in the $(\mathcal{B}, \Omega_\infty)$-plane, for different values of plant's sensitivity to toxicity $\mathcal{H}$. Results confirm the occurrence of a pitchfork bifurcation according to which, as expected, the pattern amplitude follows a square root law for $\mathcal{B} > \mathcal{B}_c$. Moreover, in line with the results previously reported in Fig. 1, it is verified that the critical value of the control parameter $\mathcal{B}_c$ is affected by $\mathcal{H}$. Indeed, when $\mathcal{H}$ is increased, the bifurcation threshold occurs for smaller values of plant loss $\mathcal{B}$. On the other hand, if rainfall $\mathcal{A}$ and plant loss $\mathcal{B}$ are kept fixed within the pattern prediction region, the migrating bands exhibit larger amplitudes for increasing values of $\mathcal{H}$, consistently with a larger distance from the instability threshold. These findings allow to strengthen the non-marginal role played by autotoxicity in the process of vegetation patterning on sloped terrains in drylands.

Finally, to validate these latter analytical results, let us address a comparison between the numerically-computed patterned solution (see Fig. 9(a)), obtained by integrating the governing system (22), and the theoretically-predicted one (see Fig. 9(b)), arising from the weakly-nonlinear analysis (18). The analysis is performed by considering a relatively close-to-onset value of the control parameter, corresponding to the small parameter $\varepsilon^2 = 10^{-2}$. The resulting satisfying agreement shown in Fig. 9 provides a definite confirmation on the validity of our theoretical predictions.

5. Concluding remarks

In this manuscript, the occurrence of oscillatory periodic vegetation patterns on sloped terrains was theoretically investigated for a class of 1D *water–biomass–toxicity* reaction–advection–diffusion systems. In particular, a quite general model was built under some assumptions regarding the

spatial dispersal mechanisms and the kinetics of the involved species. The framework here proposed accounted explicitly for the presence of toxic compounds.

Despite the autotoxicity phenomenon, which manifests itself as the impossibility for the same plant species to grow within the same region after a certain amount of time, is well-known in agriculture since ancient times, its role within the contexts of vegetation patterning has been not so deeply investigated. This is particularly true in the field of dynamics of patterns evolving on sloped terrains. With this in mind, in this work, the key features characterizing the migrating process of vegetation stripes were deduced by means of linear and weakly-nonlinear stability analyses. The analyses carried out in the above-mentioned general framework were then applied to an extension of the Klausmeier model, where the interaction between plant biomass and toxicity was explicitly taken into account.

Linear stability and, in particular, wave bifurcation analysis allowed to highlight the manifold role of plant toxicity *at the onset* of instability. Indeed, it was found that toxicity modifies the region in which oscillatory periodic patterns may be observed and affects both pattern wavelength and migration speed. In more detail, results here obtained revealed that toxicity: (i) shifts up the locus at which wave instability occurs and, to a minor extent, the locus under which the only desert state exists, so providing a destabilizing effect on the homogeneously-vegetated terrains; (ii) decreases the wavelength of vegetation bands; (iii) increases the migration speed and (iv) induces a spatial asymmetry in the profile of the vegetated band due to its different strength at the edges of the band itself. From the ecological viewpoint, the previous findings are justified by the inhibitory and noxious role that autotoxicity plays on vegetation. In fact, the presence of such a stressor into the environment yields a reduction of the overall vegetation cover and favors the transition from uniformly vegetated states to patterned ones as well as from patterned to bare grounds.

On the other hand, a multiple-scale weakly-nonlinear analysis was been carried out to gain some insights into the pattern amplitude *close-to-onset* of instability. In particular, a cubic complex Stuart–Landau equation was obtained to rule the evolution of the complex amplitude close to the bifurcating threshold and to distinguish between different dynamical regimes. This analysis allowed to prove that, as toxicity is progressively increased, a twofold effect arises: (i) a reduction of the range of rainfall values in which a subcritical regime takes place, making patterns less resilient and (ii) an increase of the pattern amplitude.

This manuscript aimed at capturing the interest of both ecologists and mathematicians involved in the study of vegetation patterns, and more generally, in the investigation of those effects caused by climate change. In this context, the role of mathematical models becomes crucial to predict the response of complex ecosystems to stressors, such as rainfall variability and plant mortality (due to human, herbivore or natural effects, as the autotoxicity), and may draw some routes toward critical scenarios, as it happens in the transition from a patterned state to a desert state.

The proposed framework lends itself to many possible extensions including: the occurrence of autotoxicity over flat terrains, where stationary patterns become oscillatory; pattern formation in 2D domains, where the pattern morphology is strongly affected by toxicity effects; "washing effects" played by water thanks to advective transport; the motion of traveling pulses driven by autotoxicity effects [40]; spatial effects arising from non-negligible diffusion of toxicity [41].

CRediT authorship contribution statement

Giancarlo Consolo: Conceptualization, Formal analysis, Funding acquisition, Investigation, Methodology, Software, Writing – original draft, Writing – review & editing. **Gabriele Grifó:** Conceptualization, Formal analysis, Investigation, Methodology, Software, Writing – original draft, Writing – review & editing. **Giovanna Valenti:** Conceptualization, Formal analysis, Investigation, Methodology, Supervision, Writing – original draft, Writing – review & editing.

Declaration of competing interest

The authors have no conflicts of interest to declare. All co-authors have seen and agree with the contents of the manuscript and there is no financial interest to report. We certify that the submission is original work and is not under review at any other publication.

Data availability

No data was used for the research described in the article.

Acknowledgments

This research was funded by MUR (Italian Ministry of University and Research) through PRIN2017 Project No. 2017YBKNCE, "Multiscale phenomena in Continuum Mechanics: singular limits, off-equilibrium and transitions", partially by PRIN2022-PNRR Project No. P2022WC2ZZ, "A multidisciplinary approach to evaluate ecosystems resilience under climate change" and by INdAM-GNFM.

Appendix. Stuart–Landau equation

In Section 3 the cubic Stuart Landau equation (16) for the complex pattern amplitude Ω has been deduced through multiple-scale weakly-nonlinear analysis:

$$\frac{\partial \Omega}{\partial T_2} = \left(\sigma_1 + \mathrm{i}\sigma_2\right)\Omega - \left(L_1 - \mathrm{i}L_2\right)|\Omega|^2\Omega \tag{A.1}$$

In the case of the extension of the Klausmeier model proposed in Section 4, the coefficients here appearing are given by:

$$\sigma_1 = \mathcal{B}_2\left\{\frac{c\left(\left.\frac{df_U^*}{d\mathcal{B}}\right|_c+\left.\frac{df_V^*}{d\mathcal{B}}\right|_c r_2\right)(n_5n_8-n_6n_7)+\left(\left.\frac{dg_S^*}{d\mathcal{B}}\right|_c r_4+\left.\frac{dg_U^*}{d\mathcal{B}}\right|_c+\left.\frac{dg_V^*}{d\mathcal{B}}\right|_c r_2\right)(n_3n_8+n_1n_7)-\left(\left.\frac{dh_S^*}{d\mathcal{B}}\right|_c r_4+\left.\frac{dh_V^*}{d\mathcal{B}}\right|_c r_2\right)(n_4n_8+n_2n_7)}{n_7^2+n_8^2}+\right.$$
$$\left.+\frac{\left(\left.\frac{dh_S^*}{d\mathcal{B}}\right|_c \hat{r}_4+\left.\frac{dh_V^*}{d\mathcal{B}}\right|_c \hat{r}_2\right)(n_4n_7-n_2n_8)-c\left.\frac{df_V^*}{d\mathcal{B}}\right|_c \hat{r}_2(n_5n_7+n_6n_8)+\left(\left.\frac{dg_S^*}{d\mathcal{B}}\right|_c \hat{r}_4+\left.\frac{dg_V^*}{d\mathcal{B}}\right|_c \hat{r}_2\right)(n_1n_8-n_3n_7)}{n_7^2+n_8^2}\right\},$$
$$\sigma_2 = \mathcal{B}_2\left\{\frac{c\left(\left.\frac{df_U^*}{d\mathcal{B}}\right|_c+\left.\frac{df_V^*}{d\mathcal{B}}\right|_c r_2\right)(n_5n_7-n_6n_8)+\left(\left.\frac{dg_S^*}{d\mathcal{B}}\right|_c r_4+\left.\frac{dg_U^*}{d\mathcal{B}}\right|_c+\left.\frac{dg_V^*}{d\mathcal{B}}\right|_c r_2\right)(n_3n_7+n_1n_8)-\left(\left.\frac{dh_S^*}{d\mathcal{B}}\right|_c r_4+\left.\frac{dh_V^*}{d\mathcal{B}}\right|_c r_2\right)(n_4n_7+n_2n_8)}{n_7^2+n_8^2}+\right. \tag{A.2}$$
$$\left.+\frac{\left(\left.\frac{dh_S^*}{d\mathcal{B}}\right|_c \hat{r}_4+\left.\frac{dh_V^*}{d\mathcal{B}}\right|_c \hat{r}_2\right)(n_4n_8-n_2n_7)-c\left.\frac{df_V^*}{d\mathcal{B}}\right|_c \hat{r}_2(n_5n_8+n_6n_7)+\left(\left.\frac{dg_S^*}{d\mathcal{B}}\right|_c \hat{r}_4+\left.\frac{dg_V^*}{d\mathcal{B}}\right|_c \hat{r}_2\right)(n_1n_7-n_3n_8)}{n_7^2+n_8^2}\right\},$$
$$L_1 = \frac{c\,m_1(n_5n_8-n_6n_7)+m_2(n_3n_8+n_1n_7)+m_3(n_4n_8+n_2n_7)+m_4(n_4n_7-n_2n_8)+c\,m_5(n_5n_7+n_6n_8)+m_6(n_1n_8-n_3n_7)}{n_7^2+n_8^2},$$
$$L_2 = \frac{c\,m_1(n_5n_7-n_6n_8)+m_2(n_3n_7+n_1n_8)+m_3(n_4n_7+n_2n_8)+m_4(n_4n_8-n_2n_7)+c\,m_5(n_5n_8+n_6n_7)+m_6(n_1n_7-n_3n_8)}{n_7^2+n_8^2},$$

where:

$$\begin{aligned}
m_1 &= \tfrac{1}{8}\,f_{UVV}\big|_c^*\left(3r_2^2+\hat{r}_2^2\right)+f_{UV}\big|_c^* r_2\left(q_{01}+q_{1r}\right)+\left(q_{02}+q_{2r}\right)\left(f_{UV}\big|_c^*+f_{VV}\big|_c^* r_2\right)+q_{1i}\hat{r}_2\left(f_{UV}\big|_c^*+f_{VV}\big|_c^*\right),\\
m_2 &= \tfrac{1}{8}\,g_{UVV}\big|_c^*\left(3r_2^2+\hat{r}_2^2\right)+g_{UV}\big|_c^*\left[q_{1i}\hat{r}_2+\left(q_{01}+q_{1r}\right)r_2+\left(q_{01}+q_{1r}\right)\right]+q_{2i}\left(g_{VS}\big|_c^*\hat{r}_3+g_{VV}\big|_c^*\hat{r}_2\right)+\\
&\quad+\left(q_{02}+q_{2r}\right)\left(g_{UV}\big|_c^*+g_{VS}\big|_c^* r_3+g_{VV}\big|_c^* r_2\right)+\left(q_{03}+q_{3r}\right)g_{VS}\big|_c^* r_2+q_{3i}\,g_{VS}\big|_c^*\hat{r}_2,\\
m_3 &= h_{VS}\big|_c^*\left[\left(q_{02}+q_{2r}\right)r_4+\left(q_{03}+q_{3r}\right)r_2+q_{2i}\hat{r}_4+q_{3i}\hat{r}_2\right],\\
m_4 &= \tfrac{1}{4}\,f_{UVV}\big|_c^* r_2\hat{r}_2+f_{UV}\big|_c^*\left[q_{1i}r_2+q_{2i}+\hat{r}_2\left(q_{01}-q_{1r}\right)\right],\\
m_5 &= \tfrac{1}{4}\,g_{UVV}\big|_c^* r_2\hat{r}_2+q_{1i}\,g_{UV}\big|_c^* r_2+\left(q_{02}-q_{2r}\right)\left(g_{VS}\big|_c^*\hat{r}_4+g_{VV}\big|_c^*\hat{r}_2\right)+\left(q_{03}-q_{3r}\right)g_{VS}\big|_c^*\hat{r}_2+q_{3i}\,g_{VS}\big|_c^* r_2+\\
&\quad+q_{2i}\left(g_{UV}\big|_c^*+g_{VS}\big|_c^* r_4+g_{VV}\big|_c^* r_2\right),\\
m_6 &= h_{VS}\big|_c^*\left[\left(q_{02}-q_{2r}\right)\hat{r}_3+\left(q_{03}-q_{3r}\right)\hat{r}_2+q_{2i}r_4+q_{3i}r_2\right],\\
n_1 &= c\,(c+\mathcal{V})\left(Y_2\hat{Y}_3-Y_3\hat{Y}_2-Y_2r_3+Y_3r_2+\hat{Y}_2r_3-\hat{Y}_3r_2\right),\\
n_2 &= (c+\mathcal{V})\left(Y_4\hat{Y}_2-Y_2\hat{Y}_4+Y_2r_4-Y_4r_2-\hat{Y}_2r_4+\hat{Y}_4r_2\right),\\
n_3 &= c\,(c+\mathcal{V})\left(Y_2\hat{r}_3-Y_3\hat{r}_2-\hat{Y}_2\hat{r}_3+\hat{Y}_3\hat{r}_2\right),\\
n_4 &= (c+\mathcal{V})\left(Y_4\hat{r}_2-Y_2\hat{r}_4+\hat{Y}_2\hat{r}_4-\hat{Y}_4\hat{r}_2\right),\\
n_5 &= \left(Y_2\hat{Y}_4-Y_4\hat{Y}_2\right)\hat{r}_3+\left(Y_3\hat{Y}_2-Y_2\hat{Y}_3\right)\hat{r}_4+\left(Y_4\hat{Y}_3-Y_3\hat{Y}_4\right)\hat{r}_2,\\
n_6 &= \left(Y_2\hat{Y}_4-Y_4\hat{Y}_2\right)r_3+\left(Y_3\hat{Y}_2-Y_2\hat{Y}_3\right)r_4+\left(Y_4\hat{Y}_3-Y_3\hat{Y}_4\right)r_2,\\
n_7 &= c\,(c+\mathcal{V})\left[\left(r_2^2+\hat{r}_2^2\right)\left(Y_3-\hat{Y}_3\right)+r_2\left(Y_2\hat{Y}_3-Y_3\hat{Y}_2\right)-\left(Y_2-\hat{Y}_2\right)\left(r_2r_3+\hat{r}_2\hat{r}_3\right)\right]+\\
&\quad+(c+\mathcal{V})\left[r_3r_2\left(Y_4-\hat{Y}_4\right)-Y_2\hat{r}_4\hat{r}_3+Y_4\hat{r}_2\hat{r}_3+\hat{Y}_2\hat{r}_4\hat{r}_3-\hat{Y}_4\hat{r}_2\hat{r}_3\right]+\\
&\quad+c\left[r_4\left(Y_2\hat{Y}_3-Y_3\hat{Y}_2\right)-r_2\left(Y_4\hat{Y}_3-Y_3\hat{Y}_4\right)\right]-r_4r_3\left(Y_2-\hat{Y}_2\right)+\mathcal{V}r_3\left(Y_2\hat{Y}_4-Y_4\hat{Y}_2\right),\\
n_8 &= (c+\mathcal{V})\left[r_4\hat{r}_3\left(\hat{Y}_2-Y_2\right)+\hat{r}_3r_2\left(Y_4-\hat{Y}_4\right)+2\hat{r}_3\left(Y_2\hat{Y}_4-Y_4\hat{Y}_2\right)-\hat{r}_2r_3\left(Y_4+\hat{Y}_4\right)+\right.\\
&\quad\left.+r_3\hat{r}_4\left(Y_2-\hat{Y}_2\right)\right]+c\,(c+\mathcal{V})\left[\left(\hat{r}_3r_2-r_3\hat{r}_2\right)\left(Y_2-\hat{Y}_2\right)+\hat{r}_2\left(Y_2\hat{Y}_3-Y_3\hat{Y}_2\right)\right]+\\
&\quad+c\left[\hat{r}_2\left(Y_4\hat{Y}_3-Y_3\hat{Y}_4\right)+\hat{r}_4\left(Y_3\hat{Y}_2-Y_2\hat{Y}_3\right)\right].
\end{aligned} \tag{A.3}$$

and

$$\begin{aligned}
Y_2 &= -\frac{\left(1-\mathcal{H}V_{R_c}\right)\left[1+V_{R_c}^2+\alpha(\mathcal{V}+c)\right]}{2\mathcal{B}}, & \hat{Y}_2 &= \frac{\beta(\mathcal{V}+c)\left(1-\mathcal{H}V_{R_c}\right)}{2\mathcal{B}},\\
Y_3 &= -\frac{\mathcal{B}\left[Y_2\left(Dc\alpha+\mathcal{H}V_{R_c}-1\right)+cD\beta\hat{Y}_2\right]}{\left(1-\mathcal{H}V_{R_c}\right)\left[(Dc\alpha-1)^2+D^2c^2\beta^2\right]}, & \hat{Y}_3 &= \frac{\mathcal{B}\left[cD\beta Y_2-\hat{Y}_2\left(Dc\alpha+\mathcal{H}V_{R_c}-1\right)\right]}{\left(1-\mathcal{H}V_{R_c}\right)\left[(Dc\alpha-1)^2+D^2c^2\beta^2\right]},\\
Y_4 &= -\alpha Y_2+\beta\hat{Y}_2, & \hat{Y}_4 &= -\alpha\hat{Y}_2-\beta Y_2,\\
r_4 &= k_c\hat{r}_2 & \hat{r}_4 &= k_cr_2\\
\alpha &= -\frac{c^3+\mathcal{V}c^2+\beta_1\big|_c c-\mathcal{V}\left(\mathcal{H}V_{R_c}-1\right)/D}{2c(\mathcal{V}+c)}, & \beta &= \sqrt{-\frac{\alpha_0\big|_c}{k_c^2c(\mathcal{V}+c)}-\alpha^2},
\end{aligned} \tag{A.4}$$

where α_0 and β_1 are defined in (5).

Finally, in (A.3), there also appear the components of the vectors

$$\mathbf{q}_0 = \begin{bmatrix} q_{01}\\ q_{02}\\ q_{03}\end{bmatrix}\in\mathbb{C}^3, \qquad \mathbf{q} = \begin{bmatrix} q_{1r}+\mathrm{i}\,q_{1i}\\ q_{2r}+\mathrm{i}\,q_{2i}\\ q_{3r}+\mathrm{i}\,q_{3i}\end{bmatrix}\in\mathbb{R}^3 \tag{A.5}$$

that occur in the approximate solution (18) and fulfill system (15).

References

[1] L. Kemp, C. Xu, J. Depledge, T.M. Lenton, Climate Endgame: Exploring catastrophic climate change scenarios, Proc. Natl. Acad. Sci. 119 (34) (2022) e2108146119, http://dx.doi.org/10.1073/pnas.2108146119.

[2] M. Rietkerk, R. Bastiaansen, S. Banerjee, J. Van De Koppel, M. Baudena, A. Doelman, Evasion of tipping in complex systems through spatial pattern formation, Science 374 (2021) http://dx.doi.org/10.1126/science.abj0359.

[3] R. HilleRisLambers, M. Rietkerk, F. van de Bosch, H.H.T. Prins, H. de Kroon, Vegetation pattern formation in semi-arid grazing systems, Ecology 82 (1) (2001) 50, http://dx.doi.org/10.1890/0012-9658(2001)082[0050:VPFISA]2.0.CO;2.

[4] M. Rietkerk, M.C. Boerlijst, F. van Langevelde, R. HilleRisLambers, J. van de Koppel, H.H.T. Prins, A. de Roos, Self-organisation of vegetation in arid ecosystems, Amer. Nat. 160 (4) (2002) 534, http://dx.doi.org/10.1086/342078.

[5] J.A. Sherratt, An analysis of vegetation stripe formation in semi-arid landscapes, J. Math. Biol. 51 (2005) 183–197, http://dx.doi.org/10.1007/s00285-005-0319-5.

[6] S. Thompson, G. Katul, S.M. McMahon, Role of biomass spread in vegetation pattern formation within arid ecosystems, Water Resour. Res. 44 (10) (2008) W10421, http://dx.doi.org/10.1029/2008WR006916.

[7] F. Borgogno, P. D'Odorico, F. Laio, L. Ridolfi, Mathematical models of vegetation pattern formation in ecohydrology, Rev. Geophys. 47 (1) (2009) RG1005, http://dx.doi.org/10.1029/2007RG000256.

[8] N. Ursino, M.C. Rulli, Combined effect of fire and water scarcity on vegetation patterns in arid lands, Ecol. Model. 221 (19) (2010) 2353–2362, http://dx.doi.org/10.1016/j.ecolmodel.2010.06.018.

[9] S. van der Stelt, A. Doelman, G. Hek, J.D.M. Rademacher, Rise and fall of periodic patterns for a generalized Klausmeier-Gray-Scott model, J. Nonlinear Sci. 23 (7) (2013) 39–95, http://dx.doi.org/10.1007/s00332-012-9139-0.

[10] A. Marasco, A. Iuorio, F. Cartení, G. Bonanomi, D.M. Tartakovsky, S. Mazzoleni, F. Giannino, Vegetation pattern formation due to interactions between water availability and toxicity in plant-soil feedback, Bull. Math. Biol. 76 (11) (2014) 2866–2883, http://dx.doi.org/10.1007/s11538-014-0036-6.

[11] K. Siteur, E. Siero, M.B. Eppinga, J.D.M. Rademacher, A. Doelman, M. Rietkerk, Beyond Turing: The response of patterned ecosystems to environmental change, Ecol. Complex. 20 (2014) 81–96, http://dx.doi.org/10.1016/j.ecocom.2014.09.002.

[12] E. Meron, Nonlinear Physics of Ecosystems, first ed., CRC Press, Boca Raton, 2015, http://dx.doi.org/10.1201/b18360.

[13] G. Consolo, C. Curró, G. Valenti, Pattern formation and modulation in a hyperbolic vegetation model for semiarid environments, Appl. Math. Model. 43 (3) (2017) 372–392, http://dx.doi.org/10.1016/j.apm.2016.11.031.

[14] G. Consolo, C. Curró, G. Valenti, Supercritical and subcritical Turing pattern formation in a hyperbolic vegetation model for flat arid environments, Physica D 398 (11) (2019) 141–163, http://dx.doi.org/10.1016/j.physd.2019.03.006.

[15] G. Consolo, G. Valenti, Secondary seed dispersal in the Klausmeier model of vegetation for sloped semi-arid environments, Ecol. Model. 402 (2019) 66–75, http://dx.doi.org/10.1016/j.ecolmodel.2019.02.009.

[16] L. Eigentler, J.A. Sherratt, An integrodifference model for vegetation patterns in semi-arid environments with seasonality, J. Math. Biol. 81 (2020) 875–904, http://dx.doi.org/10.1007/s00285-020-01530-w.

[17] G. Consolo, C. Curró, G. Valenti, Turing vegetation patterns in a generalized hyperbolic Klausmeier model, Math. Methods Appl. Sci. 43 (18) (2020) 10474, http://dx.doi.org/10.1002/mma.6518.

[18] G. Consolo, G. Grifó, Eckhaus instability of stationary patterns in hyperbolic reaction-diffusion models on large finite domains, Partial Differ. Equ. Appl. 3 (2022) 57, http://dx.doi.org/10.1007/s42985-022-00193-0.

[19] G. Consolo, C. Curró, G. Grifó, G. Valenti, Oscillatory periodic pattern dynamics in hyperbolic reaction–advection–diffusion models, Phys. Rev. E 105 (2022) 034206, http://dx.doi.org/10.1103/PhysRevE.105.034206.

[20] G. Consolo, G. Grifó, G. Valenti, Dryland vegetation pattern dynamics driven by inertial effects and secondary seed dispersal, Ecol. Model. 474 (2022) 110171, http://dx.doi.org/10.1016/j.ecolmodel.2022.110171.

[21] G. Grifó, Vegetation patterns in the hyperbolic Klausmeier model with secondary seed dispersal, Mathematics 11 (2023) 1084, http://dx.doi.org/10.3390/math11051084.

[22] G. Grifó, G. Consolo, C. Curró, G. Valenti, Rhombic and hexagonal pattern formation in 2D hyperbolic reaction-transport systems in the context of dryland ecology, Physica D 449 (2023) 133745, http://dx.doi.org/10.1016/j.physd.2023.133745.

[23] G. Consolo, G. Grifó, Turing vegetation patterns in flat arid environments with finite soil carrying capacity, Ric. Mat. (2023) http://dx.doi.org/10.1007/s11587-023-00783-z.

[24] C. Curró, G. Grifó, G. Valenti, Turing patterns in hyperbolic reaction-transport vegetation models with cross-diffusion, Chaos Solitons Fractals 176 (2023) 114152, http://dx.doi.org/10.1016/j.chaos.2023.114152.

[25] S. Mazzoleni, G. Bonanomi, F. Giannino, M. Rietkerk, S. Dekker, F. Zucconi, Is plant biodiversity driven by decomposition processes? An emerging new theory on plant diversity, Community Ecol. 8 (1) (2007) 103–109, http://dx.doi.org/10.1556/ComEc.8.2007.1.12.

[26] S. Mazzoleni, G. Bonanomi, G. Incerti, M.L. Chiusano, P. Termolino, A. Mingo, M. Senatore, F. Giannino, F. Cartení, M. Rietkerk, V. Lanzotti, Inhibitory and toxic effects of extracellular self-DNA in litter: A mechanism for negative plant-soil feedbacks? New Phytol. 205 (3) (2014) 1195–1210, http://dx.doi.org/10.1111/nph.13121.

[27] J. von Hardenberg, E. Meron, M. Shachak, Y. Zarmi, Diversity of vegetation patterns and desertification, Phys. Rev. Lett. 87 (2001) 198101, http://dx.doi.org/10.1103/PhysRevLett.87.198101.

[28] F. Cartení, A. Marasco, G. Bonanomi, S. Mazzoleni, M. Rietkerk, F. Giannino, Negative plant soil feedback explaining ring formation in clonal plants, J. Theoret. Biol. 313 (2012) 153–161, http://dx.doi.org/10.1016/j.jtbi.2012.08.008.

[29] K. Gowda, H. Riecke, M. Silber, Transitions between patterned states in vegetation models for semi-arid ecosystems, Phys. Rev. E 89 (2014) 022701, http://dx.doi.org/10.1103/PhysRevE.89.022701.

[30] A. Marasco, F. Giannino, A. Iuorio, Modelling competitive interactions and plant–soil feedback in vegetation dynamics, Ric. Mat. 69 (2020) 553—577, http://dx.doi.org/10.1007/s11587-020-00497-6.

[31] L. Eigentler, J.A. Sherratt, Long-range seed dispersal enables almost stationary patterns in a model for dryland vegetation, J. Math. Biol. 86 (2023) 15, http://dx.doi.org/10.1007/s00285-022-01852-x.

[32] A. Marasco, A. Iuorio, F. Cartení, G. Bonanomi, F. Giannino, S. Mazzoleni, Water limitation and negative plant-soil feedback explain vegetation patterns along rainfall gradient, Procedia Environ. Sci. 19 (2013) 139–147, http://dx.doi.org/10.1016/j.proenv.2013.06.016.

[33] A. Iuorio, F. Veerman, The influence of autotoxicity on the dynamics of vegetation spots, Physica D 427 (2021) 133015, http://dx.doi.org/10.1016/j.physd.2021.133015.

[34] K. Spiliotis, L. Russo, F. Giannino, C. Siettos, Numerical bifurcation analysis of turing and symmetry broken patterns of a vegetation pde model, arXiv. http://dx.doi.org/10.48550/arXiv.2303.13248.

[35] M.C. Thompson, P. Le Gal, The Stuart–Landau model applied to wake transition revisited, Eur. J. Mech. B Fluids 23 (2004) 219–228, http://dx.doi.org/10.1016/j.euromechflu.2003.09.012.

[36] D. Kondrashov, M.D. Chekroun, P. Berloff, Multiscale Stuart-Landau emulators: Application to wind-driven ocean gyres, Fluids 3 (1) (2018) 21, http://dx.doi.org/10.3390/fluids3010021.

[37] C.A. Klausmeier, Regular and irregular patterns in semiarid vegetation, Science 284 (5421) (1999) 1826–1828, http://dx.doi.org/10.1126/science.284.5421.1826.

[38] COMSOL Multiphysics®, Ver 6.0 COMSOL AB, Stockholm, Sweden, 2010, URL https://www.comsol.com/.

[39] W. van Saarloos, P.C. Hohenberg, Pulses and fronts in the complex Ginzburg-Landau equation near a subcritical bifurcation, Phys. Rev. Lett. 64 (1990) 749–752, http://dx.doi.org/10.1103/PhysRevLett.64.749.

[40] G. Grifó, A. Iuorio, F. Veerman, Far-from-equilibrium travelling pulses in sloped semi-arid environments driven by autotoxicity effects, in preparation.

[41] A. Iuorio, M.B. Eppinga, M. Baudena, F. Veerman, M. Rietkerk, F. Giannino, Modelling how negative plant–soil feedbacks across life stages affect the spatial patterning of trees, Sci. Rep. 13 (1) (2023) 19128, http://dx.doi.org/10.1038/s41598-023-44867-0.